Role of solar wind turbulence in the coupling of the solar wind to the Earth's magnetosphere

Joseph E. Borovsky
Space and Atmospheric Science Group, Los Alamos National Laboratory, Los Alamos, New Mexico, USA

Herbert O. Funsten
Center for Space Science and Exploration, Los Alamos National Laboratory, Los Alamos, New Mexico, USA

Received 22 July 2002; revised 25 September 2002; accepted 12 March 2003; published 20 June 2003.

[1] The correlation between the amplitude of the MHD turbulence in the upstream solar wind and the amplitude of the Earth's geomagnetic activity indices AE, AU, AL, Kp, ap, Dst, and PCI is explored. The amplitude of the MHD turbulence is determined by the fluctuation amplitude of the solar wind magnetic field. This "turbulence effect" in solar wind/magnetosphere coupling is more easily discerned when the interplanetary magnetic field (IMF) is northward, but the effect is also present when the IMF is southward. The magnitude of the effect is the same for northward and southward IMF, accounting for about 150 nT of the variability of the AE index. Tests are performed that conclude (1) that the turbulence effect is not caused by the turbulence amplitude acting as a proxy for $|B|$ in the solar wind and (2) that reversals of the IMF from northward to southward in the turbulent fluctuations is not the cause of the correlations. An expression is derived for the total viscous-shear force on the surface of the magnetosphere; improved solar wind/magnetosphere correlations result when this expression is used. With insight from fluid-flow experiments, the turbulence effect is interpreted as an enhanced viscous coupling of the solar wind flow to the Earth's magnetosphere caused by an eddy viscosity that is controlled by the amplitude of MHD turbulence in the upstream solar wind: more upstream turbulence means more momentum transfer from the magnetosheath into the magnetosphere, resulting in more stirring of the magnetosphere, which produces enhanced geomagnetic activity indices. *INDEX TERMS:* 2784 Magnetospheric Physics: Solar wind/magnetosphere interactions; 2722 Magnetospheric Physics: Forecasting; 2149 Interplanetary Physics: MHD waves and turbulence; 7863 Space Plasma Physics: Turbulence; *KEYWORDS:* freestream turbulence, solar wind/magnetosphere coupling, eddy viscosity, Reynold's stress, viscous drag, astrophysical flows

Citation: Borovsky, J. E., and H. O. Funsten, Role of solar wind turbulence in the coupling of the solar wind to the Earth's magnetosphere, *J. Geophys. Res.*, *108*(A6), 1246, doi:10.1029/2002JA009601, 2003.

1. Introduction

[2] The supersonic, superAlvenic, solar wind interacts with the dipole magnetic field of the Earth, which forms an impenetrable obstacle. Given a geometry for a fluid-flow problem, the key parameter to describe the phenomenology of the flow pattern and the coupling of the flow to boundaries and obstacles is the Reynolds number

$$Re = v_0 L/\nu_{\mathrm{kin}}, \tag{1}$$

a dimensionless number constructed from a typical velocity v_0 in the flow, a typical lengthscale L for the geometry, and the kinematic viscosity ν_{kin} of the fluid. The solar wind, the magnetosheath, and the magnetosphere are high Reynolds number systems. For these hot, low-density plasma flows, the kinematic viscosities ν_{kin} are in the 10^3–10^6 cm^2/s range (cf. equation 2.23 of *Braginskii* [1965] and see Table 1), the flow velocities v_0 are in the tens to hundreds of kilometer per second range, and the scale sizes L_0 are in the 10^4–10^7 km range, the Reynolds numbers $Re = v_0 L_0/\nu_{\mathrm{kin}}$ are in the 10^{12}–10^{14} range (see Table 1). Similarly, with electrical conductivities in the 10^{14}–10^{17}/s range [see section 5.2.3.3 of *Alfven and Falthammar*, 1963], the magnetic Reynolds numbers,

$$Re_m = v_0 L 4\pi\sigma/c^2, \tag{2}$$

of these flows are extremely large. As expected for high Reynolds number systems [*Montgomery*, 1987], the convection is not smooth but is dominated by fluctuations and the magnetic fields are distorted. This is true of the solar wind [e.g., *Tu and Marsch*, 1995], of the magnetosheath [e.g., *Sonett and Abrams*, 1963; *Safrankova et al.*, 2000], and of the magnetosphere [e.g., *Borovsky et al.*, 1997]. Despite the fact that the magnetosphere and the solar wind are extremely high Reynolds number plasmas, investigations into the phenomenology and consequences of turbulence in magnetospheric physics are rare [*Haerendel*, 1978; *Montgomery*, 1987; *Antonova and Ovchinnikov*, 1996; *Borovsky et al.*, 1997; *Zelenyi et al.*, 1998; *White et al.*, 2001; *Borovsky and Funsten*, 2003].

[3] As is the case for ordinary fluids [see sections 1.4 and 7.1 of *Tennekes and Lumley*, 1972; *Townsend*, 1976; *Smits and Dussauge*, 1996], turbulence in the MHD flows of the solar wind, magnetosheath, and magnetosphere may produce enhanced mixing and enhanced momentum transport which can lead to gross changes in the large-scale flow patterns. Following a suggestion of *Borovsky and Gosling* [2001], in this report one possible effect of turbulence will be explored: the enhanced viscous coupling of the magnetosheath to the magnetosphere owed to an eddy viscosity controlled by the level of MHD turbulence in the upstream solar wind.

2. An Experiment of Interest for Solar-Terrestrial Physics

[4] The suggestion of *Borovsky and Gosling* [2001] is that there would be a positive correlation between the level of geomagnetic activity and the amplitude of the MHD turbulence in the solar wind. This suggestion was motivated by the results of high Reynolds number wind-tunnel experiments in which fluids interact with obstacles (spheres, cylinders, airfoils, and blades) placed in the flows (see Figure 1). The magnetosphere's interaction with the solar wind has analogies with the interaction of an object with a fluid flow [cf. *Borovsky et al.*, 1998]. One must of course be aware of the limitations of using fluid experiments to make inferences about the solar wind/magnetosphere system: fluids do not include many plasma effects, and the obstacles in fluid experiments are not magnetic dipoles. One must also be aware of the limitations of our MHD simulation tools for studying the solar wind/magnetosphere problem, like an inability to include boundary layer processes, and most pertinent here, restrictively low Reynolds numbers owing to numerical diffusivity and poor grid resolution. Each approach can yield insights but not the complete story.

Table 1. Typical Turbulence and Plasma Parameters for the Solar Wind, the Magnetosheath, and the Magnetotail[a]

	Solar Wind	Magnetosheath	Magnetotail
δv, km/s	14	40	75
δB, nT	3	12	7
$\delta v/v_0$	0.03	0.2	5
$\delta B/B_0$	0.5	0.5	0.5
n, cm^{-3}	7	25	0.3
T_i, keV	0.01	1	7
T_e, keV	0.01	0.2	1
β	0.75	15	5
ν_{kin}, cm^2/s	1.6×10^6	5.6×10^4	1.2×10^3
σ, s^{-1}	1.9×10^{14}	1.6×10^{16}	1.6×10^{17}
v_0, km/s	400	200	15
L (R_E)	5000	5	6
Re	1×10^{14}	1×10^{12}	5×10^{12}
Re_m	3×10^{14}	1×10^{13}	1×10^{13}

[a]Note that the values of all three vary considerably from day to day.

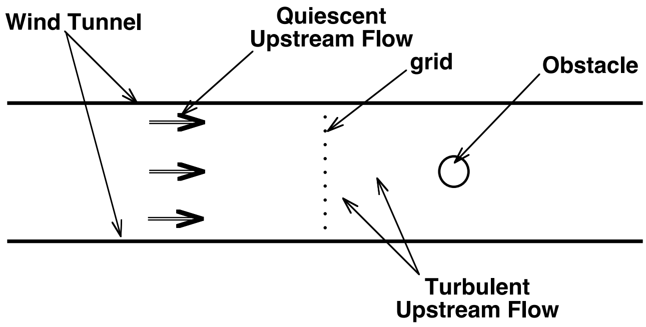

Figure 1. A sketch of a typical experiment to study the effect of upstream turbulence on the coupling of a fluid flow to an obstacle in the flow.

[5] Ordinarily, in obstacle-in-flow experiments, care is taken to ensure that the level of turbulence in the upstream flow is minimal. Among other things, this helps to ensure a reproducibility to the experiments [see section 8 of *Seeger*, 1967] and helps to simplify the interpretation of results. In some recent experiments (see Figure 1), grids were placed upstream of the obstacles to inject controlled levels of turbulence into the upstream fluid. Changing the properties of the grids changed the properties of the upstream turbulence. The interaction of the fluid flow with the obstacle was studied versus the amplitude of the upstream (freestream) turbulence. Some results are summarized in Table 2.

[6] One observed consequence is an increase in the viscous drag (= skin friction) on an obstacle produced by an increase in the amplitude of the upstream turbulence [*Blair*, 1983a, 1983b; *Pal*, 1985]. This enhanced viscous drag comes about from an eddy viscosity (= turbulent viscosity = Reynolds stress) that is owed to the velocity fluctuations in the upstream fluid; this eddy viscosity can transfer momentum across boundary layers, which adds to the momentum transport to a surface. As depicted in Figure 2, the skin friction can increase by several tens of percent when turbulence intensities $\delta v/v_0$ increase by less than 10%, where δv is the rms fluctuation velocity upstream and v_0 is the mean flow velocity relative to the obstacle [*Blair*, 1983b].

[7] A second consequence is a shortening of the wake behind an obstacle produced by an increase in the amplitude of the upstream turbulence [*Castro and Robins*, 1977; *Pal*, 1985; *Wu and Faeth*, 1994a; *Zhang and Han*, 1995; *Murawaski and Vafai*, 2000]. The wake reduction with an increase in freestream turbulence is caused by an increase in the eddy diffusion, which increases the transport of momentum perpendicular to the flow into the wake region from the flow outside.

[8] A third consequence is the alteration of the total drag force on an obstacle in a flow associated with an increase in the amplitude of the upstream turbulence [*Courchesne and Laneville*, 1982; *Hoffmann*, 1991; *Littman et al.*, 1996]. Since the total drag force is the sum of a viscous drag and a pressure drag, there are two competing effects that come into play when the intensity of the upstream turbulence is increased. Owing to an increase in the eddy viscosity, the viscous drag increases. However, owing to an increase in

Table 2. Summary of the Effects of Upstream Turbulence in Fluid Experiments

	Less Upstream Turb.	More Upstream Turb.	References
Skin friction	less viscous drag	more viscous drag	*Blair*, 1983a, 1983b; *Pal*, 1985
Wake length	wake downstream longer	wake downstream shorter	*Castro and Robins*, 1977; *Pal*, 1985; *Wu and Faeth*, 1994a; *Zhang and Han*, 1995; *Murawaski and Vafai*, 2000
Pressure drag	more pressure drag	less pressure drag	*Courchesne and Laneville*, 1982; *Hoffmann*, 1991; *Littman et al.*, 1996
ν_{eddy}	less eddy viscosity	more eddy viscosity	*Volino*, 1998; *Wu and Faeth*, 1994a, 1994b; *Pal*, 1985
Re_{eff}	higher effective Reynolds	lower effective Reynolds	*Volino*, 1998; *Wu and Faeth*, 1994a, 1994b

the eddy diffusion, the flow void behind an obstacle is filled more effectively and so the pressure difference between the front and back of the obstacle is reduced, resulting in a reduction in the pressure drag. For most obstacle shapes, the latter effect is greater and the total drag force on an obstacle is reduced by an increase of the amplitude of the upstream turbulence. Obstacle shapes such as the Earth's magnetosphere that have tapered downstream regions (e.g., obstacles with aft fairings) tend to have significantly reduced pressure drag at the expense of slightly enhanced viscous drag [*Hoerner*, 1965; *Snyder et al.*, 2000].

[9] In parameterizing the effects of the level of upstream turbulence, it is convenient to calculate the eddy viscosity [*Tennekes and Lumley*, 1972; *Borovsky et al.*, 1997]

$$\nu_{\mathrm{eddy}} = C_\nu \delta v^2 \tau_{\mathrm{auto}} \tag{3}$$

from the amplitude δv and correlation time τ_{auto} of the upstream velocity fluctuations (with C_ν being a constant coefficient of size 0.06–0.09) and then add this eddy viscosity to the molecular kinematic viscosity ν_{kin} of the fluid to obtain a total viscosity, and then to construct an "effective" Reynolds number Re_{eff} from this total viscosity

$$Re_{\mathrm{eff}} = v_0 L / \left(\nu_{\mathrm{kin}} + \nu_{\mathrm{eddy}}\right) \tag{4}$$

[e.g., *Volino*, 1998; *Wu and Faeth*, 1994b]. For wakes produced behind obstacles in turbulent flows, *Wu and Faeth* [1994a, 1994b] found that the wakes, which were themselves turbulent and which changed with changes in the amplitudes of the upstream turbulence, when time averaged appeared to be similar to laminar wakes at Reynolds numbers equal to the effective Reynolds numbers calculated accounting for the upstream-turbulence eddy viscosity. The replacement of ν_{kin} by $\nu_{\mathrm{kin}} + \nu_{\mathrm{eddy}}$ in the fluid equations works well for numerically simulating freestream-turbulence experiments with the use of laminar-flow computer schemes [*Volino*, 1998]. Such a technique, when properly implemented, may be pertinent to efforts to numerically simulate the solar wind driven magnetosphere with low Reynolds number MHD codes that cannot reproduce the turbulence that is seen in satellite data [cf. *Yoshizawa*, 1991; *Theobalk et al.*, 1994; *Agullo et al.*, 2001].

[10] The amplitude of upstream turbulence is of concern for several practical applications: the lift and drag of aircraft wings [*Hoffmann*, 1991; *Huang and Lee*, 1999], the wind forces on buildings and structures [*Barriga et al.*, 1977; *Zdravkovich and Carelas*, 1997], air drag on automobiles [*Bearman*, 1978], drag and heat transfer from turbine blades [*Fridman*, 1997; *Murawaski and Vafai*, 2000], forces on underwater structures [*Torum and Anand*, 1985], and the settling of particles suspended in fluids [*Brucato et al.*, 1998]. This report will focus on the first finding listed in Table 2, the increase of the viscous drag (skin friction) with an increase in the amplitude of the upstream turbulence, with application to the solar wind/magnetosphere flow problem.

3. Eddy-Viscosity Hypothesis

[11] The physical interpretation of the fluid experiments of section 2 is that the upstream turbulence produces an eddy viscosity in the fluid and that this eddy viscosity acts in addition to molecular viscosity to couple the fluid flow to the obstacles [*Wu and Faeth*, 1994b; *Volino*, 1998]. With an understanding that the solar wind is not a simple fluid, but with a hope that high Reynolds number fluid experiments can compliment our low Reynolds number MHD computer-simulation capability to provide unique insights about the

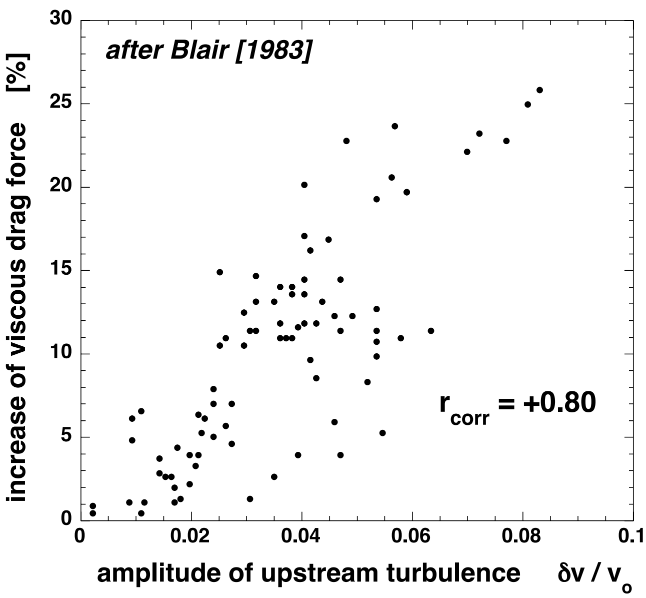

Figure 2. From a flat plate in a wind tunnel, the increase in the viscous drag force (= skin friction) of the wind on the plate is plotted as a function of the amplitude of the upstream turbulence (after Figure 3 of *Blair* [1983b]).

solar wind driving of the magnetosphere, the hypothesis that there is an increase in the viscous interaction between the solar wind and the magnetosphere with an increase in the amplitude of solar wind turbulence is investigated in this report.

[12] One quantitative measure of the coupling of the solar wind to the magnetosphere is the strength of the current systems measured by the various geomagnetic activity indices [e.g., *Kamide and Slavin*, 1986]. As suggested by *Borovsky and Gosling* [2001], if there is an enhanced viscous interaction controlled by the amplitude of the turbulence in the solar wind, then there should be correlations between the solar wind turbulence amplitude and the geomagnetic indices. Although largely ignored at present, such correlations have been found in the past [*Ballif et al.*, 1967, 1969; *Hirshberg and Colburn*, 1969; *Bobrov*, 1973; *Garrett*, 1974; *Garrett et al.*, 1974]. Two physical interpretations of these correlations have been given. (1) That the correlations are owed to a filter effect wherein AC electric fields of the solar wind are able to penetrate into the magnetosphere better than DC electric fields [*Garrett et al.*, 1974], so when solar wind fluctuations are larger, the dawn-to-dusk solar wind electric field gets into the magnetosphere more effectively and so the solar wind can drive the magnetosphere harder. (2) That the fluctuations of the solar wind produce locally enhanced surface currents at the magnetopause which drives magnetic field line reconnection harder [*Schindler*, 1979], which enhances the total reconnection rate leading to a stronger driving of the magnetosphere by the solar wind. Both of these interpretations are consistent with a turbulence effect acting to increase the geomagnetic indices when the interplanetary magnetic field (IMF) is southward, but not acting when the IMF is northward.

[13] The hypothesis addressed in this report is that the correlations between the amplitude of the solar wind turbulence and the geomagnetic indices owe to an eddy-viscosity effect. A test of this hypothesis is that the turbulence effect on the geomagnetic indices should be present both for northward and southward IMF. That test is performed in the following section.

4. Correlations Between Solar Wind Turbulence Amplitudes and Geomagnetic Activity Indices

[14] To examine the correlations between solar wind quantities and the geomagnetic indices of the Earth, 3 years of OMNI solar wind data are used, 1979–1981, supplemented by hourly averaged values of the auroral-electrojet indices AE, AL, and AU [*Rostoker*, 1972], and the polar cap index PCI (Thule) [*Troishichev et al.*, 1988]. The OMNI data set contains the indices Kp and Dst and the ap index can be constructed from the values of Kp using Table 6 of *Mayaud* [1980]. The OMNI data [*Papitashvili et al.*, 2000] was constructed by converting high time resolution solar wind flow and magnetic field measurements into hourly averaged quantities. For 1979–1981, the OMNI data are almost exclusively from ISEE-3 and IMP-8. The OMNI solar wind measurements are time shifted from the solar wind satellite (typically ISEE-3) to the Earth using the solar wind convection velocity. As an indicator of the level of turbulence in the solar wind, the standard deviations of the magnetic field measurements going into each of the hourly averages is used. Two measures of the amplitude of the turbulence are constructed from these standard deviations. The first measure is δB_{yz}, which is defined as $\delta B_{yz} = [(\sigma B_y)^2 + \sigma B_z)^2]^{1/2}$, where σB_y is the standard deviation of the B_y values going into the hourly average and where σB_z is the standard deviation of the B_z values going into the hourly average. The y and z directions are both approximately normal to the direction of flow of the solar wind. The second measure is $\delta B_{yz}/B$, where B is the hourly averaged magnitude of the solar wind magnetic field. For the purposes of this study, it is unimportant which measure of turbulence amplitude is used: the various measures that can be constructed from the magnetic field fluctuations are all highly correlated with each other. As shown in Appendix A, the hourly averaged values of δB_{yz} in the solar wind have autocorrelation time of $\sim$5 hours, similar to the autocorrelation time for the hourly averaged values of vB_z. This $\sim$5-hour autocorrelation time is caused by the time variation of the amplitude of the solar wind MHD turbulence. The time series of δB_{yz} values also has a component with a faster autocorrelation time ($\sim$1 hour in the OMNI data, $\sim$5 min when examined with higher time resolution solar wind data: see Appendix A). This fast-autocorrelation-time component is probably owed to the presence of rotational and tangential discontinuities in the solar wind, as discussed in Appendix A.

[15] To ensure that the standard deviations of the magnetic field measurements are not constructed from only a few measurements, hourly averages that used less than 60 time samples are removed. Additionally, to ensure that the standard deviations of the field measurements are not anomalously high because of shock waves in the solar wind, 3-hour-long intervals were removed around 127 interplanetary shocks, with the shock times supplied by J. Gosling (private communication, 2002) from his survey of ISEE-3 satellite data. The first of these cleaning procedures eliminates the ISEE-3 data in the OMNI data set from the study, leaving the IMP-8 magnetic field measurements with $\sim$15 s time resolution to be used to calculate δB_{yz} and the hourly averaged values of B and B_z. The two cleaning procedures together remove $\sim$61% of the OMNI hourly averaged data in 1979–1981. As discussed in Appendix A, rotational/tangential discontinuities are not removed.

[16] As an indicator of the level of turbulence in the solar wind, the level of magnetic field fluctuations is used, whereas in upstream-turbulence experiments in the laboratory the level of velocity fluctuations is used. Unfortunately, owing to the difficulties in measuring the flow velocity of the solar wind plasma to sufficient accuracy, the standard deviations of the flow-velocity fluctuations in the OMNI data set is not an adequate measure of the turbulence amplitude. However, in MHD, magnetic field fluctuations cannot occur without velocity fluctuations [e.g., section 7.2 of *Parker*, 1979]. In the solar wind, the amplitude of velocity fluctuations is in general tied to the amplitude of the magnetic field fluctuations (cf. Figure 8 of *Matthaeus and Goldstein* [1982] or Figure 4 of *Roberts et al.* [1990]) and a measurement of one is equivalent to a measurement of the other. With a time resolution of 15 s, the 1-hour averages of the standard deviations of the magnetic field measurements pick up frequencies in the 10^{-4}–10^{-2} Hz range, which is in the inertial range of the solar wind MHD

turbulence [*Leamon et al.*, 1998; *Smith et al.*, 2001]. Since the spectral shape of the inertial range is a constant, measuring the amplitude of the turbulence in one frequency band suffices to measure the intensity of the turbulence (C. Smith, private communication, 2002). Note that even if there were magnetic field fluctuations with no velocity fluctuations, the Reynolds-averaged MHD equations still have a kinetic Reynolds stress [cf. *Yoshizawa and Yokoi*, 1996; *Fontan*, 1999], i.e., they still have an eddy viscosity that depends on the amplitude of the magnetic field fluctuations.

[17] In Figure 3 the various geomagnetic indices are plotted as functions of vB_z of the solar wind. A large amount of scatter in the data have been removed in this figure by sorting the data with respect to vB_z and then performing 1000-point running statistical analyses of the indices, which uncovers trends that underlie scatter in the data points. As can be seen, for vB_z positive, which is B_z positive and which is IMF northward, there is not much dependence of the indices on vB_z, but for vB_z negative, which is B_z negative and which is IMF southward, the magnitudes of the indices increase as the magnitude of vB_z increases, noting that AL and Dst are negative. Because the behaviors of the indices differ for northward and for southward IMF, and because the vB_z effect on the indices is so strong, the coupling of the solar wind to the magnetosphere is examined separately for northward and southward IMFs.

[18] Two subsets of data are extracted from the 3 years of OMNI data plus geomagnetic indices, one subset for a northward-IMF regime with 1000 nT km/s < vB_z < 3000 nT km/s and one subset for a southward-IMF regime with 1000 nT km/s < $-vB_z$ < 3000 nT km/s. For the two subsets, the various linear correlation coefficients r_{corr} (see Appendix B) between the driver quantities vB_z, δB_{yz}, $\delta B_{yz}/B$, and B and the geomagnetic activity indices AE, AL, AU, Kp, Dst, ap, and PCI are displayed in Table 3 (northward) and Table 4 (southward). Correlation at the 95% confidence level occurs for correlation coefficients $>2/N^{1/2}$ [e.g., section IX of *Beyer*, 1966; section 4.8.1 of *Bendat and Piersol*, 1971], where N is the number of points used to calculate the linear correlation. (See also Appendix B for a discussion of this confidence level.) For the ∼1700 data points in each subset, definite correlation occurs for correlation coefficients greater than ∼±4.8%. As can be seen by comparing the two tables, vB_z is a strong driver of the geomagnetic indices (i.e., there is a significantly nonzero correlation coefficient) for southward IMF (Table 4), but vB_z is not so clearly a driver for northward IMF (Table 3). This is as expected (see Figure 3). The two measures of turbulence amplitude in the solar wind, δB_{yz} and $\delta B_{yz}/B$, have significant correlation with the geomagnetic indices AE, AL, AU, Kp, ap, and PCI, both for northward and for southward IMF, with the correlation being stronger (or clearer) for northward IMF. Note that all of the turbulence-measure correlations are well beyond the ±4.8% level.

[19] The increases in the geomagnetic activity indices with increasing amplitudes of solar wind turbulence are shown in Figure 4 for northward IMF. To see the trends underlying scatter in the data, the hourly averaged data is sorted according to the level of turbulence δB_{yz} and then 200-point running averages of the indices are performed. From Tables 3 and 4 and Figure 4 it can be concluded that

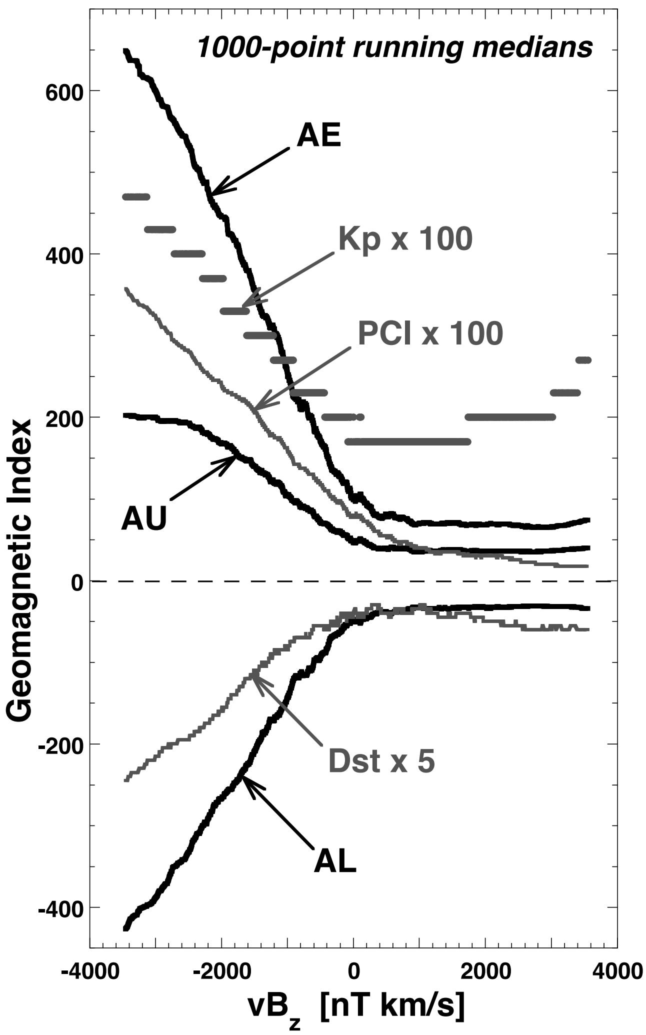

Figure 3. The various geomagnetic activity indices are plotted as function of vB_z of the solar wind. The hourly averaged data is sorted by vB_z and then 1000-point running medians are calculated. Note that the Kp index has discrete values. The ap index, which has a behavior very similar to Kp, is not shown. Note also that there is zero time lag between the solar wind and the indices in this figure.

the amplitude of the turbulence in the upstream solar wind does affect the geomagnetic indices of the Earth, with geomagnetic activity increasing as the level of turbulence increases. This conclusion is particularly clear for northward IMF. This is consistent with the hypothesis that enhanced turbulence upstream leads to enhanced coupling of the solar wind to the magnetosphere.

[20] As can be seen in Figure 4, the variation of δB_{yz} contributes to about 150 nT of the variability of the AE index. Looking at Figure 3, this 150 nT is smaller than the several hundred nanotesla variability of AE associated with the variation of vB_z. Using the 200-point running averages of Figure 4, the sizes of the ranges of variation of the hourly averaged indices AE, AL, AU, and PCI as δB_{yz} varies under northward IMF are shown in the first column of Table 5. Then 200-point running averages of the indices versus vB_z are constructed (similar to the 1000-point running medians of Figure 3) and the sizes of the ranges of variation of the

Table 3. Linear Cross-Correlation Coefficients r_{corr} (In Percent) Between Driver Functions (Columns) and Geomagnetic Activity Indices (Rows) for Northward Interplanetary Magnetic Field (1000 nT km/s < vB_z < 3000 nT km/s)[a]

	vB_z	δB_{yz}	$\delta B_{yz}/B$	B
AE	−3.3	+33.6	+23.9	+17.2
AL	+3.1	−27.9	−19.8	−13.9
AU	−3.2	+36.2	+25.8	+19.3
Kp	+10.9	+45.8	+34.4	+22.8
Dst	−7.9	−11.4	−5.7	−11.1
ap	+10.4	+41.8	+28.0	+22.5
PCI	−8.5	+31.5	+18.8	+21.9

[a]One thousand six hundred fifty-six points go into each correlation, and the 95% confidence level of correlation is ±5.0%. There is no time lag between the solar wind quantities and the geomagnetic activity indices.

indices as vB_z varies under southward IMF are calculated and shown in the second column of Table 5. To compare the amount of variation owed to the turbulence effect versus the amount of variation owed to vB_z, the ratios of the ranges are taken (column 2 divided by column 3) and these ratios (in percent) are displayed in the fourth column of Table 5. As can be seen, the variation in the geomagnetic indices caused by the level of solar wind turbulence is a few tens of percent as large as the variation caused by vB_z. Note that there is a significant difference in the ratio for AL and for AU; the turbulence effect is much more important for AU than it is for AL. For AU the turbulence effect is ~44% of the size of the vB_z effect. (Note in Table 3 too that for the drivers δB_{yz} and $\delta B_{yz}/B$, the correlation coefficients are higher for AU than they are for AL under northward IMF.) AU is sometimes considered to be a measure of the directly driven response of the dayside magnetosphere and AL is a measure of the directly driven plus loading-unloading response of the nightside magnetosphere [e.g., *Goertz et al.*, 1993].

[21] Note in Tables 3 and 4 that the correlations between the turbulence amplitudes and the Dst index are weak at best. The Dst index is a measure of the amount of plasma pressure in the inner magnetosphere [*Rostoker*, 1972; *Liemohn et al.*, 2001], whereas the other indices are measures of convective activity in the outer magnetosphere. As will be seen below, the correlation between the amplitude of the solar wind turbulence and Dst improves if a several-hour time lag is introduced between the solar wind measurements and the measurement of Dst.

[22] As can be seen in Tables 3 and 4, there are significant correlations between the magnitude B of the solar wind magnetic field and the geomagnetic indices. Note also in Tables 3 and 4 that the correlations between δB_{yz} and the geomagnetic indices are higher than the correlations between $\delta B_{yz}/B$ and the geomagnetic indices. There are strong positive correlations between the turbulence amplitude δB_{yz} and the magnitude B: for the northward-IMF data the correlation is +34.6% and for the southward-IMF data it is +39.1%. To ensure that the correlations of the geomagnetic indices with

Table 4. Linear Cross-Correlation Coefficients r_{corr} (In Percent) Between Driver Functions (Columns) and Geomagnetic Activity Indices (Rows) for Southward Interplanetary Magnetic Field (1000 nT km/s < $-vB_z$ < 3000 nT km/s)[a]

	vB_z	δB_{yz}	$\delta B_{yz}/B$	B
AE	−44.5	+15.2	+7.0	+20.8
AL	+44.3	−13.6	−6.6	−16.7
AU	−30.7	+13.1	+5.4	+21.0
Kp	−46.1	+39.4	+27.1	+35.7
Dst	+32.6	−7.4	−1.5	−17.6
ap	−42.3	+39.2	+23.8	+36.6
PCI	−38.5	+12.1	+4.1	+18.1

[a]One thousand seven hundred forty-two points go into each correlation, and the 95% confidence level of correlation is ±4.8%. There is no time lag between the solar wind quantities and the geomagnetic activity indices.

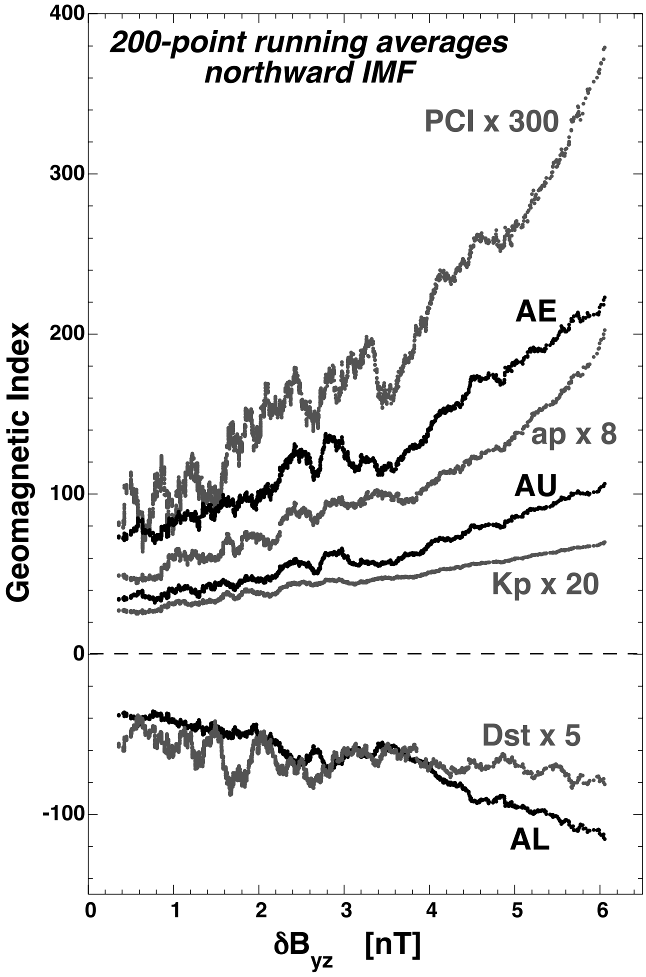

Figure 4. For northward interplanetary magnetic field (IMF) (1000 nT km/s < vB_z < 3000 nT km/s) the various geomagnetic activity indices are plotted as functions of the amplitude of upstream turbulence δB_{yz} in the solar wind. The hourly averaged data is sorted by δB_{yz} and then 200-point running averages are performed.

Table 5. For 200-Point Running Averages of the Data, the Range of Variation of the Hourly Indices AE, AL, AU, and PCI are Shown for δB_{yz} Under Northward Interplanetary Magnetic Field (Second Column) and for vB_z Under Southward Interplanetary Magnetic Field (IMF) (Third Column)[a]

	Range of Variation With δB_{yz} for Northward IMF	Range of Variation With vB_z for Southward IMF	Ratio of δB_{yz} Variation to vB_z Variation, %
AE	150 nT	670 nT	22
AL	79 nT	493 nT	16
AU	72 nT	164 nT	44
PCI	1.0	3.8	26

[a]The ranges are compared in the fourth column.

δB_{yz} are not owed to a magnitude of B effect in the driving of the geomagnetic indices, the effect of B on the indices is removed and the correlations with δB_{yz} are then rechecked. To remove the magnitude of B effect, the OMNI data is selected for a limited range of B (8 nT < B < 10 nT), and the correlations between the drivers and the geomagnetic activity indices are repeated. The results appear in Table 6 for northward IMF (1000 nT km/s < vB_z < 3000 nT km/s), where the turbulence-amplitude effect is clearest. As can be seen in Table 6, restricting B removes any significant correlations between the indices and B, but the correlations of the indices with the turbulence amplitude remain. Hence the correlations between the amplitude δB_{yz} of the solar wind turbulence and the geomagnetic activity indices are not owed to a magnitude of B effect, where δB_{yz} acts as a proxy for B.

[23] Another effect to check against is the possibility that the correlations between the amplitude of turbulence and the geomagnetic indices are owed to fraction-of-an-hour long southward turnings of the IMF even though the hourly averaged value of B_z is northward. Larger amplitudes of turbulence would have a larger likelihood of a B_z reversal and hence the stronger driving of the magnetosphere for larger amplitudes of turbulence. This would be a high-frequency analogy of the HILDCAA effect (see, for example, Figure 12 of *Tsurutani et al.* [1995]). A test as to whether this B_z-reversal effect is responsible for the correlations between the amplitude of the solar wind turbulence under northward IMF and the AE index is performed as follows. Only data where the hourly averaged value of B_z is positive (northward) is retained and $\sigma B_z/\langle B_z\rangle$ is calculated, where σB_z is the standard deviation of all B_z values during the hour and $\langle B_z\rangle$ is the average value of B_z for the hour. A value of $\sigma B_z/\langle B_z\rangle$ much greater than unity means that during that hour it was likely that there was a brief interval of southward IMF even though the hourly average of B_z was positive. A value of $\sigma B_z/\langle B_z\rangle$ much less than unity means that during that hour it was very unlikely that there was a brief interval of southward IMF. That is, for values $\sigma B_z/\langle B_z\rangle \ll 1$ the B_z-reversal effect is ruled out as a cause of any correlation between δB_{yz} and AE. The linear correlation coefficient r_{corr} between δB_{yz} and AE is calculated for various restricted ranges of $\sigma B_z/\langle B_z\rangle$ and the correlation coefficient is plotted in Figure 5. As can be seen, if the correlation is plotted between δB_{yz} and AE for essentially all values of $\sigma B_z/\langle B_z\rangle$ that occur (right-hand edge of graph) a correlation coefficient of 0.339 (= 33.9%) is obtained. As the values of $\sigma B_z/\langle B_z\rangle$ are restricted to smaller and smaller values (moving toward the left on the graph), the correlation coefficient r_{corr} is reduced. For values of $\sigma B_z/\langle B_z\rangle$ < 0.75, reversals of B_z into the southward-B_z regime are unlikely (as indicated on the figure). In this range of $\sigma B_z/\langle B_z\rangle$ values a correlation between δB_{yz} and AE remains, but the correlation coefficient r_{corr} is weaker than the correlation coefficient for the full range of $\sigma B_z/\langle B_z\rangle$ values. But then, the variance $\sigma^2(\delta B_{yz})$ of δB_{yz} values is also reduced, so a reduced correlation coefficient is expected [cf. *Pagano*, 1981]. The question is, is the correlation coefficient r_{corr} less than expected for the reduced range of δB_{yz} variance? To answer this, a gedanken experiment is performed (Figure 6). Here a string of points $x = y$ is taken with a range $x = -50$ to $x = +50$. This string of points has a perfect correlation. Gaussian-distributed random numbers (with Gaussian halfwidths of 25) are then added to both the x and y values to reduce the perfect correlation. Then for various ranges of x values the linear correlation coefficient r_{corr} between x and y is calculated and plotted. Also, plotted is the variance $\sigma^2(x)$ of the x values in the restricted range of x values. As can be seen in the graph of Figure 6, when all of the x values are used (right-hand edge of the graph) the correlation between x and y is $r_{\text{corr}} = 0.537$ (= 53.7%) and as the range of x values used is reduced (moving toward the left in the graph) the correlation coefficient r_{corr} is reduced. Simultaneously, the variance of the x values $\sigma^2(x)$ is reduced. If the ratio $r_{\text{corr}}/\sigma(x)$ is taken (open circles), it is seen that this ratio does not vary

Table 6. Removing the B Effect to See if There Remains a Turbulence-Level Effect[a]

	All Values of B			8 nT < B < 10 nT		
	B	δB_{yz}	$\delta B_{yz}/B$	B	δB_{yz}	$\delta B_{yz}/B$
AE	+17.2	+33.6	+23.9	+5.2	+39.6	+39.0
AL	−13.9	−27.9	−19.8	−2.9	−34.2	−34.1
AU	+19.3	+36.2	+25.8	+7.8	+42.9	+41.8
Kp	+22.8	+45.8	+34.4	+7.1	+50.8	+50.5
Dst	−11.1	−11.4	−5.7	−3.2	−9.1	−3.6
ap	+23.5	+41.8	+28.0	+7.4	+40.6	+39.8
PCI	+22.0	+31.5	+18.8	−2.1	+39.0	+39.5

[a]Linear cross-correlation coefficients are in percent. Northward interplanetary magnetic field (IMF), where the turbulence effect is clearest.

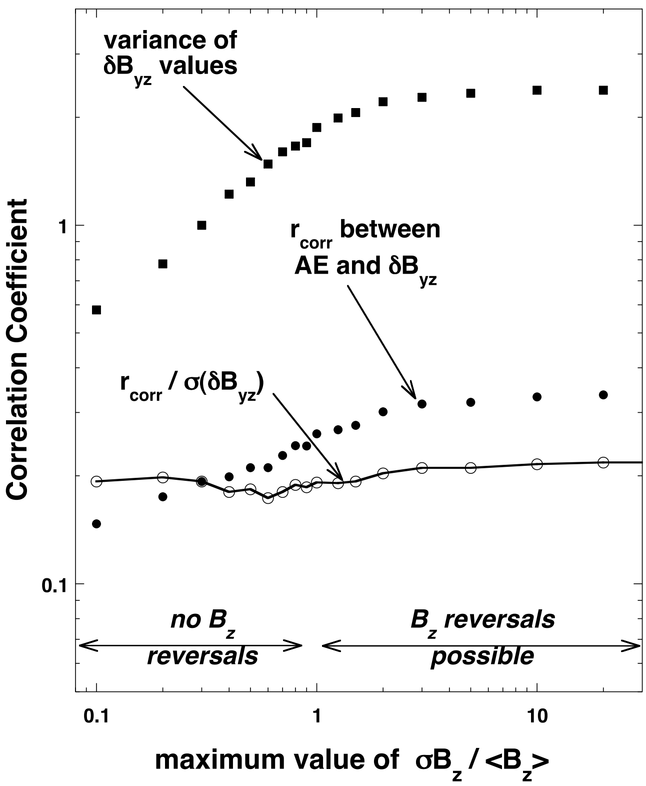

Figure 5. For northward interplanetary magnetic field (IMF), the correlation coefficient r_{corr} between δB_{yz} and AE is plotted as a function of the maximum value of $\sigma B_z/\langle B_z\rangle$ allowed, where $\langle B_z\rangle$ is the hourly average of B_z in the solar wind and σB_z is standard deviation of B_z measurements in that hour. Also, plotted is the variance $\sigma^2(\delta B_{yz})$ of δB_{yz} values and $r_{\text{corr}}/\sigma(\delta B_{yz})$ as functions of the maximum allowed value of $\sigma B_z/\langle B_z\rangle$.

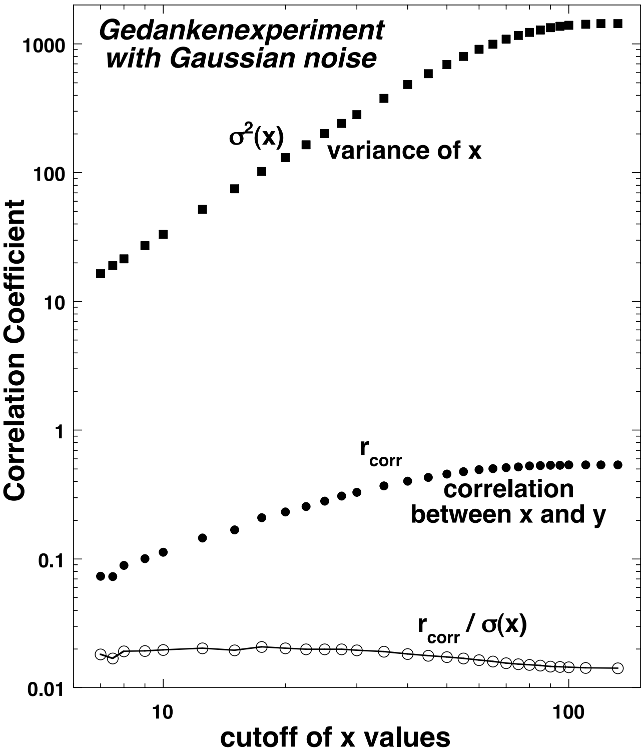

Figure 6. A gendanken experiment is performed in which Gaussian noise is added to a set of perfectly correlated x and y values to lower the correlation coefficient (to 53.7%) owing to noise. Then the range of x values is restricted to examine how the correlation coefficient between x and y is reduced in comparison to the reduction in the variance of x values.

significantly as the range of x values is reduced. Hence for noisy data, as the range of x values is reduced the correlation coefficient is expected to be reduced but the ratio of $r_{corr}/\sigma(x)$ should not be reduced. Now looking again at the δB_{yz}-AE correlation results in Figure 5, the ratio $r_{corr}/\sigma(\delta B_{yz})$ is plotted as the open circles. As can be seen, this ratio remains approximately constant as the range of $\sigma B_z/\langle B_z\rangle$ is reduced and the correlation coefficient between δB_{yz} and AE is reduced. This is the amount of reduction of r_{corr} that should be expected if the correlation between δB_{yz} and AE remains. Hence it is concluded that the reduction in the correlation between δB_{yz} and AE is caused purely by the reduction in the variance of δB_{yz} values used to calculate the correlation: it is not caused by the removal of a B_z-reversal effect. This means that a B_z-reversal effect is not the cause of the enhanced coupling between the solar wind and the magnetosphere associated with an enhanced amplitude of solar wind turbulence when the IMF is northward.

[24] In the IMF-northward and IMF-southward regimes, multivariate linear-regression fits of the AE index as a function of vB_z and δB_{yz} are performed. The best fit for northward IMF (1000 nT km/s < vB_z < 3000 nT km/s) is

$$\mathrm{AE} = -0.0123 vB_z + 25.5\delta B_{yz} + 66.3, \tag{5}$$

with a linear correlation coefficient r_{corr} of 34.2%. In expression (5) AE, δB_{yz}, and vB_z are in nT km/s. The linear-correlation coefficient for the bivariate fit AE-vB_z is 3.3% and for the bivariate fit AE-δB_{yz} it is 33.6%. For northward IMF, adding vB_z information improves the AE-δB_{yz} fit. For southward IMF (1000 nT km/s < $-vB_z$ < 3000 nT km/s) the best fit is

$$\mathrm{AE} = -0.169 vB_z + 18.2\delta B_{yz} + 81.5, \tag{6}$$

with a linear-correlation coefficient r_{corr} of 46.3%. Again, AE is in nT, δB_{yz} is in nT, and vB_z is in nT km/s. The linear-correlation coefficient for the bivariate fit AE-vB_z is 44.5% and for the bivariate fit AE-δB_{yz} it is 15.2%. For southward IMF, adding δB_{yz} information improves the AE-vB_z fit. For southward IMF, vB_z dominates over δB_{yz} for driving the AE index, whereas for northward IMF δB_{yz} dominates over vB_z for driving the AE index. Note that the linear coefficients between AE and δB_{yz} are similar (25.5 and 18.2) in expressions (5) and (6), indicating that the turbulence-amplitude effect which is clearly discernible for northward IMF is similar under northward and southward IMF: it is roughly $\partial(\mathrm{AE})/\partial(\delta B_{yz}) \approx 22$, where both the AE index and δB_{yz} are measured in nT. This type of slope can be seen in Figure 4.

[25] The fact that the turbulence effect on AE has the same magnitude for northward IMF as it does for southward IMF is graphically demonstrated in Figures 7 and 8. Here linear-regression fits to AE as a function of vB_z are plotted for four groups of data: the combination of northward IMF ($0 < vB_z < 3000$ nT km/s) or southward IMF ($0 < -vB_z <$ 3000 nT km/s) and low-level turbulence ($\delta B_{yz}/B < 0.1$) or high-level turbulence ($\delta B_{yz}/B > 0.5$). These linear-regression

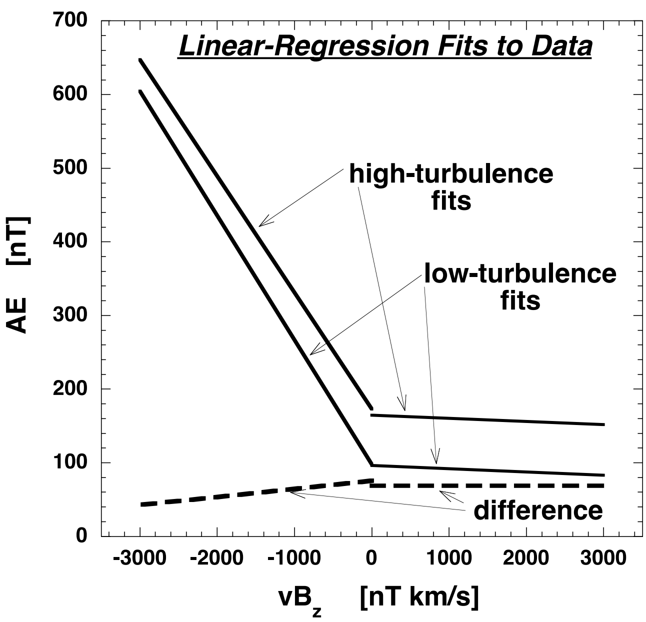

Figure 7. Four linear-regression fits (solid curves) to the AE versus vB_z data. The fits are for $0 < vB_z < 3000$ (northward interplanetary magnetic field (IMF)) and $0 < -vB_z < 3000$ (southward IMF) for $\delta B_{yz}/B < 10\%$ (low-level turbulence) and $\delta B_{yz}/B > 50\%$ (high-level turbulence). The weak-turbulence curves are subtracted from the high-turbulence curves to see how the level of turbulence affects AE (dashed curves).

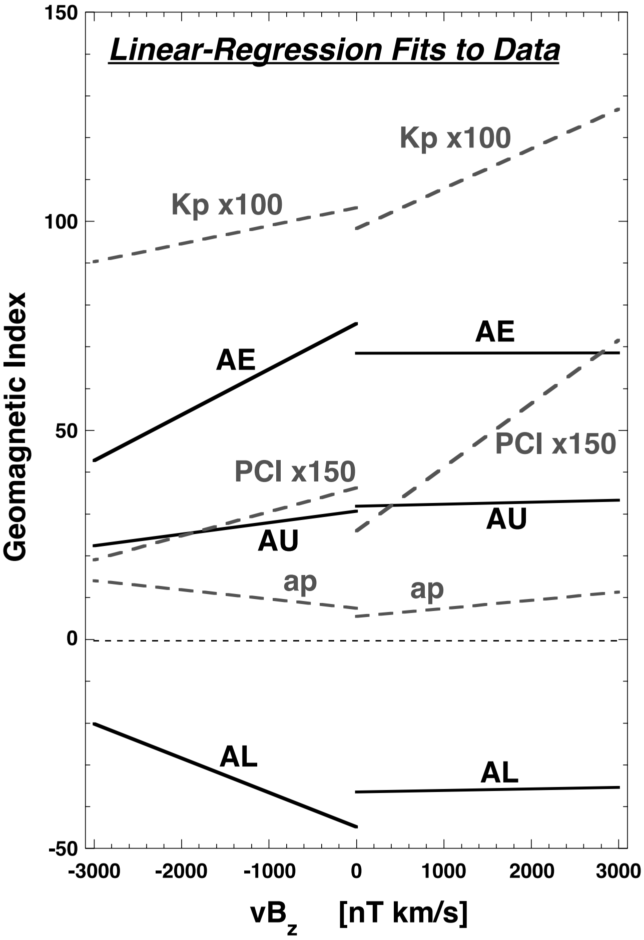

Figure 8. As in Figure 7, difference curves are produced for AE, AU, AL, Kp, ap, and PCI by subtracting high-turbulence-level linear-regression fits from low-turbulence-level linear-regression fits.

fits are the four solid curves in Figure 7. Then the two low-turbulence curves are subtracted from the two high-turbulence curves to produce the two dashed curves, which represent the change in AE owed to an increase in the level of turbulence. As can be seen, this turbulence-effect increase in AE is similar for northward IMF and southward IMF. Repeating this procedure for the other geomagnetic indices, the resulting six pairs of difference curves are plotted in Figure 8. As can be seen, for AE, AU, AL, Kp, ap, and PCI, the turbulence effect on each index is similar for northward and southward IMF. Figure 8 also indicates that about 70 nT of the AE index is associated with switching from low $\delta B_{yz}/B$ to high $\delta B_{yz}/B$, as is $\sim$30 nT of AU, $\sim$30 nT of AL, $\sim$1 unit of Kp, $\sim$0.3 units of PCI, and $\sim$10 units of ap.

[26] The linear-correlation coefficients between the amplitude of the solar wind turbulence and the various geomagnetic indices are plotted as functions of the time lag between the solar wind measurements (velocity shifted to Earth) and the measurements of the indices in Figures 9 and 10. A positive time lag means the magnetospheric index responds "after" a change in the solar wind. Figure 9 uses δB_{yz} as a measure of the turbulence amplitude and Figure 10 uses $\delta B_{yz}/B$ as a measure. As can be seen, for the various indices (excepting Dst) a time lag of about 1 hour optimizes the correlation. This may indicate a reaction time of about 1 hour for those geomagnetic indices to fully respond to a change in the level of turbulence bathing the magnetosphere. The cross-correlation times between the level of turbulence and the various geomagnetic indices, which are the characteristic falloff times of the curves in the figure, are about 5–9 hours. As indicated in Appendix A, the autocorrelation times for δB_{yz} and $\delta B_{yz}/B$ in the solar wind are about 9 and 7 hours, respectively. Hence the cross-correlation times in Figures 9 and 10 probably reflect the autocorrelation times of the solar wind drivers.

[27] To summarize the findings of this examination of the correlations between the amplitude of turbulence in the upstream solar wind and the various geomagnetic indices (the turbulence effect), it was found that (1) the turbulence effect operates for both northward and southward IMF (see Tables 3 and 4), (2) the strength of the turbulence effect is the same for northward and for southward IMF (see expressions (1) and (2) and Figures 7 and 8), (3) for northward IMF the turbulence effect is not caused by reversals of B_z associated with the turbulent fluctuations (see Figures 5 and 6), (4) the amplitude of the turbulence is not acting as a proxy for $|B|$ in the correlations (Table 6), and (5) the optimal time lag between the solar wind and the magnetospheric indices for the turbulence effect is about 1 hour.

[28] The interpretation of these results is that there is an eddy-viscous interaction between the solar wind and the magnetosphere that is controlled by the level of turbulence in the upstream solar wind. Louder upstream turbulence leads to a larger eddy viscosity (= a larger Reynolds stress), which leads to more momentum transport from the solar wind flow into the magnetosphere, which leads to greater convection in the magnetosphere, which drives stronger current systems between the magnetosphere and the ionosphere, and which leads to elevated geomagnetic indices.

5. Comparison of Eddy Viscosity and Reconnection

[29] The turbulence effect can be compared to the vB_z reconnection driver of the magnetosphere by honing in on the physics of eddy viscosity and the viscous driving of the magnetosphere. First, viscous driving is examined.

[30] The drag force $F_{\rm drag}$ on an obstacle in a fluid flow can be written [e.g., *Faber*, 1995]

$$F_{\rm drag} = (1/2)\rho u_\infty^2 \left(\pi d^2/4\right) C_D \qquad (7)$$

where C_D is the drag coefficient, ρ is the mass density of the fluid, u_∞ is the upstream flow velocity, and d is the cross-stream "diameter" of the obstacle. (In this chapter and in Appendix C, u is chosen for velocity rather the v to avoid confusion with viscosity ν.) The total drag force $F_{\rm drag}$ (known also as the profile drag) is the sum of two components $F_{\rm drag} = F_{\rm visc} + F_{\rm press}$, a viscous drag (known also as the skin friction) $F_{\rm visc}$ and a pressure drag (known also as the form drag) $F_{\rm press}$ (see, e.g., equations (9.2)–(9.4) of *Nakamura and Boucher* [1999]). Likewise, the dimensionless drag coefficient $C_D = C_{\rm visc} + C_{\rm press}$ is the sum of two dimensionless coefficients, a viscous-drag coefficient $C_{\rm visc}$ (often called C_f in the literature) and a pressure-drag coefficient $C_{\rm press}$ (often called $C_{\rm form}$ in the literature). With

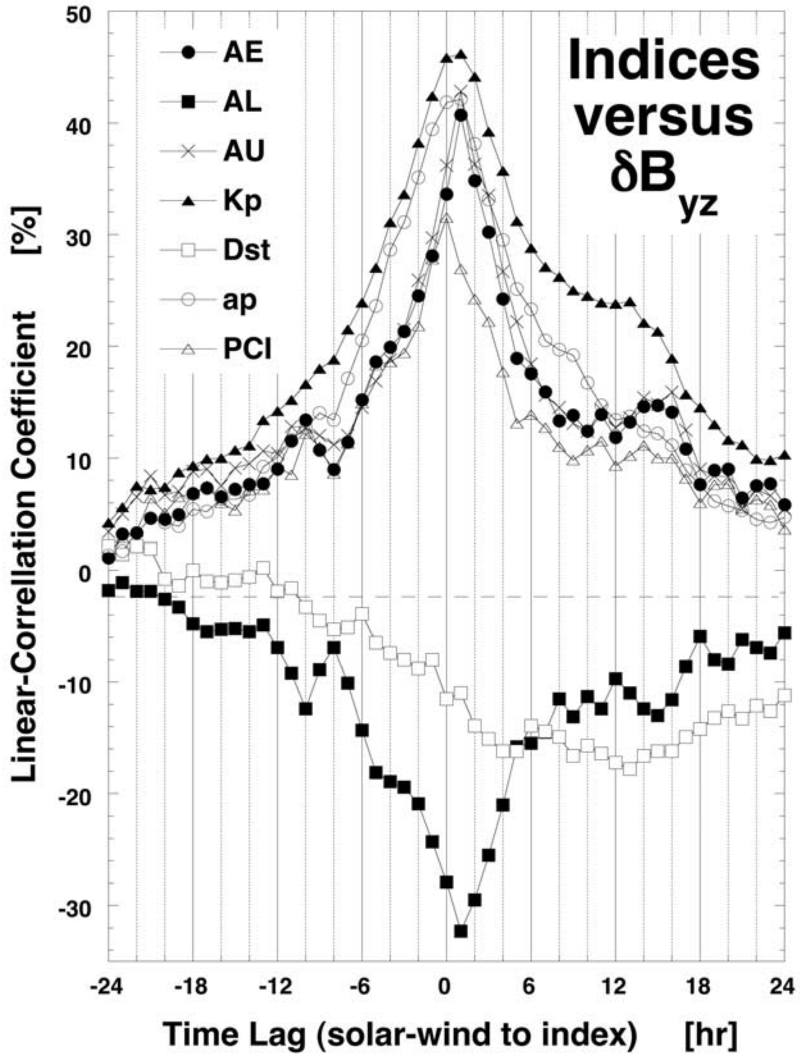

Figure 9. The linear-correlation coefficient between δB_{yz} in the solar wind and the various geomagnetic activity indices is plotted as a function of the time lag from the solar wind to the magnetospheric index. Note that the solar wind measurements are time shifted to Earth at the solar wind convection velocity.

these definitions used in expression (7), the viscous drag force on an obstacle in a flow is

$$F_{\rm visc} = (1/2)\rho u_\infty^2 \left(\pi d^2/4\right) C_{\rm visc} \tag{8}$$

The coefficient of viscous drag $C_{\rm visc}$ depends on the shape of the obstacle and the Reynolds number of the flow past the obstacle (i.e., the geometry and the Reynolds number). For a blunt-body obstacle such as the magnetosphere, the appropriate Reynolds number is

$$Re = u_\infty d/\nu_{\rm kin} = u_\infty 2r/\nu_{\rm kin}, \tag{9}$$

where d is the diameter of the obstacle in the direction normal to the flow and $\nu_{\rm kin}$ is the kinematic viscosity of the fluid. Ordinarily, the molecular kinematic viscosity or the Braginskii viscosity is used for $\nu_{\rm kin}$, but later in this section an eddy viscosity will be used for ν. Using an eddy viscosity puts the Reynolds number of the magnetosheath flow past the magnetosphere in the $Re = 10–10^6$ range. For a rough estimate of the coefficient of viscous drag $C_{\rm visc}$ for the magnetosphere, $C_{\rm visc}$ for a spherical obstacle could be taken. For $10 \leq Re \leq 10^6$, a theoretical value for a sphere is $C_{\rm visc} \sim 5Re^{-1/2}$ (e.g., equation (7.25) of *Faber* [1995]) and numerical solutions of the Navier-Stokes boundary layer equations for a sphere yield $C_{\rm visc} = 6.3Re^{-1/2}$ for $10^2 \leq Re \leq 10^4$ (e.g., Table 1 of *El-Shaarawi et al.* [1997]). Full simulations of the Navier-Stokes equation at Reynolds numbers $Re \leq 10^3$ support these values [*Dennis and Walker*, 1971; *Feng and Michaelides*, 2001]. Taking the magnetosphere to be shaped as a hemisphere attached to the end of a cylinder, a better estimate of $C_{\rm visc}$ for the magnetosphere is derived in Appendix C. It is

$$C_{\rm visc} = 13.3Re^{-1/2}. \tag{10}$$

As noted in Appendix C, if internal convection of the magnetosphere occurs as a result of the viscous interaction, then the factor 13.3 in expression (10) would be somewhat lessened. Inserting the coefficient of viscous drag expression (10) into expression (8) and using expression (9) for Re yields

$$F_{\rm visc} = 5.22\rho u_\infty^{3/2} d^{3/2} \nu_{\rm kin}^{1/2}. \tag{11}$$

Now for the eddy viscosity.

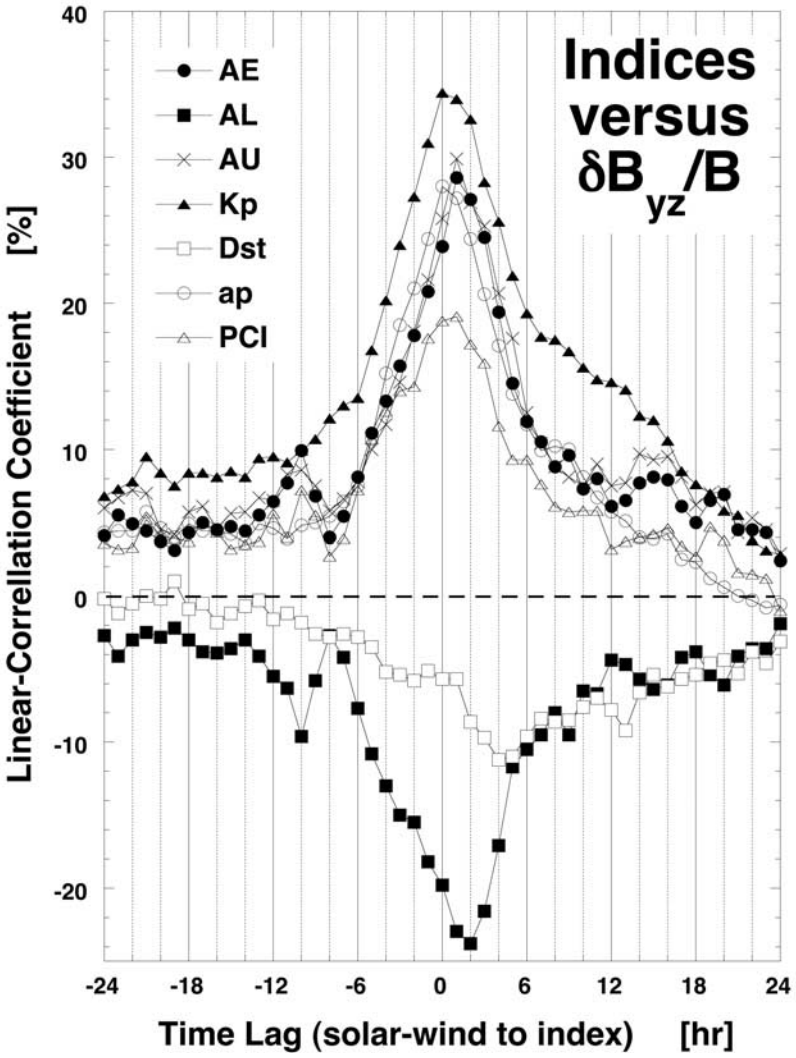

Figure 10. The linear-correlation coefficient between $\delta B_{yz}/B$ in the solar wind and the various geomagnetic activity indices is plotted as a function of the time lag from the solar wind to the magnetospheric index. Note that the solar wind measurements are time shifted to Earth at the solar wind convection velocity.

[31] Following the prescription of *Wu and Faeth* [1994b] and *Volino* [1998] for the analysis of experiments with eddy viscosity controlled by the level of upstream turbulence, the kinematic viscosity ν_{kin} in the Reynolds number is replaced by an effective viscosity $\nu_{\mathrm{eff}} = \nu_{\mathrm{kin}} + \nu_{\mathrm{eddy}} \approx \nu_{\mathrm{eddy}}$. The eddy viscosity is taken to be $\nu_{\mathrm{eddy}} = C\nu(\delta u)^2\tau_{\mathrm{corr}}$ (expression (3)), where δu is the amplitude of velocity fluctuations in the turbulent flow and τ_{corr} is the correlation time of the velocity fluctuations in the turbulence. The reader is cautioned that this eddy-viscosity expression is a rough approximation that comes from a fluid-turbulence mixing-length theory. Only the amplitude δu^2 of the velocity fluctuations are taken into account whereas for MHD turbulence the eddy-viscosity expression should also contain a term that is proportional to the amplitude of the magnetic field fluctuations δB^2 of the turbulence (e.g., equation (2.21a) of *Chen and Montgomery* [1987] or equation (26) of *Fontan* [1999]). Since the magnetic field fluctuation energy and the velocity-fluctuation kinetic energy are approximately equal, this correction is anticipated to be on the order 1. Taking $\delta u \approx u_\infty(\delta B/B)$ in $\nu_{\mathrm{eddy}} = C_\nu(\delta u)^2\tau_{\mathrm{corr}}$, where $\delta B/B$ is a measure of the amplitude of the turbulence, and taking the coefficient C_ν in expression (3) to be $C_\nu \approx 0.06$ [*Hamba*, 1992; *Yoshizawa and Yokoi*, 1996; sections 7.1.3 and 10.4.1 of *Pope*, 2000], expression (9) becomes the effective Reynolds number

$$Re_{\mathrm{eff}} = u_\infty d/\nu_{\mathrm{eddy}} = 16.6du_\infty^{-1}(\delta B/B)^{-2}\tau_{\mathrm{corr}}^{-1}. \tag{12}$$

Using this expression for ν_{eddy} in expression (11) yields

$$F_{\mathrm{visc}} \approx 1.28\rho u_\infty^{5/2}(\delta B/B)\tau_{\mathrm{corr}}^{1/2}d^{3/2}. \tag{13}$$

If the correlation time τ_{corr} of the turbulence does not vary appreciably with the amplitude of the turbulence, and if the diameter d of the magnetosphere does not vary appreciably, then (writing $\rho = m_p n$, where m_p is the proton mass, and replacing the symbol u_∞ with v)

$$F_{\mathrm{visc}} \propto nv^{5/2}\left(\delta B_{yz}/B\right), \tag{14}$$

where n is the number density of the solar wind, v is the velocity of the solar wind and $\delta B_{yz}/B$ is a measure of the turbulence amplitude of the upstream solar wind.

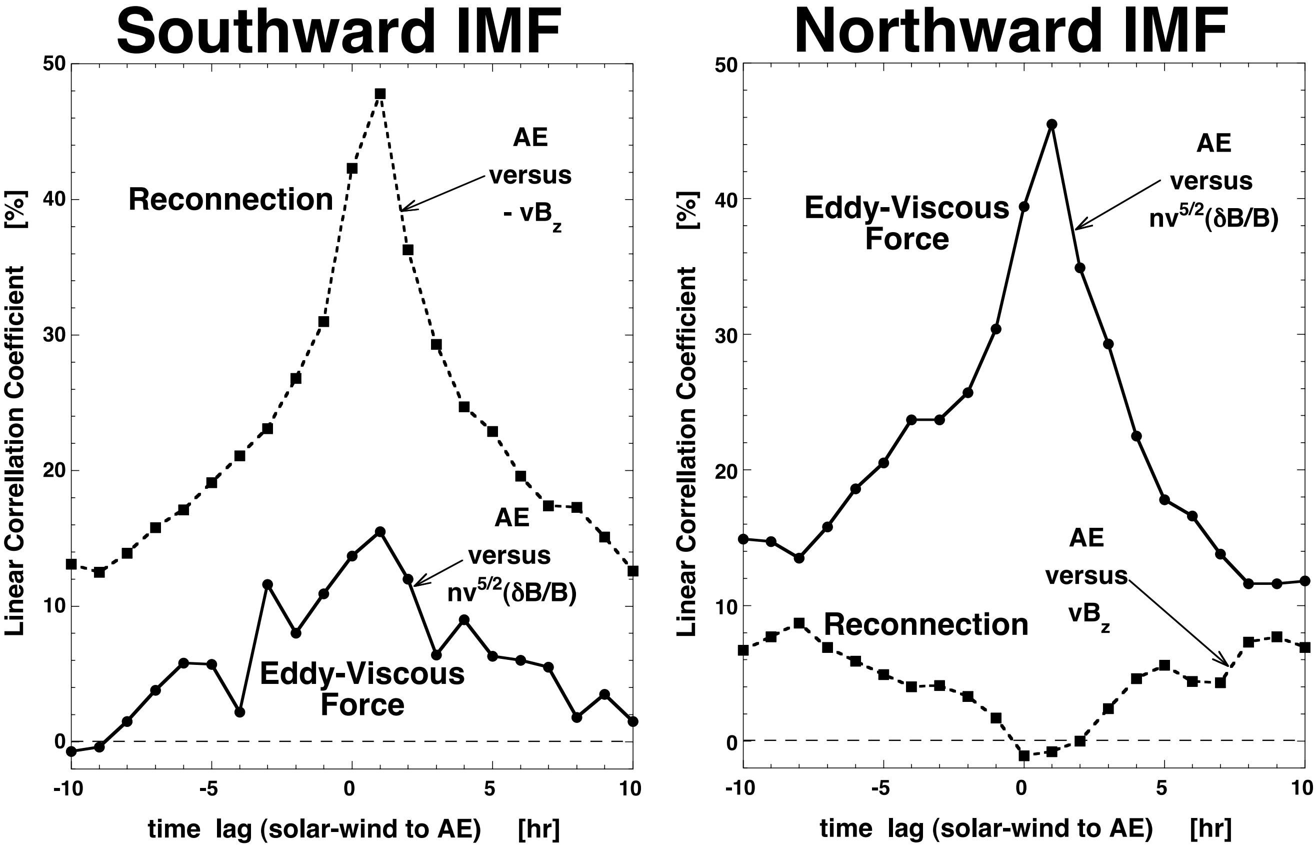

Figure 11. The cross correlation between the AE index and two quantities in the solar wind: vB_z and $nv^{5/2}(\delta B/B)$. The correlation between AE and vB_z is an indicator of reconnection driving of the magnetosphere and the correlation between AE and $nv^{5/2}(\delta B/B)$ is an indicator of the eddy viscous driving of the magnetosphere. For northward interplanetary magnetic field (IMF) the eddy-viscous driving dominates the variation of AE (second panel) and for southward IMF reconnection dominates the variation of AE (first panel).

[32] The total viscous force of the solar wind on the magnetosphere should scale with the solar wind parameters of expression (14). This eddy-viscous driver is compared with the reconnection driver vB_z in the two panels of Figure 11. Here the linear correlation coefficient between each driver and AE is plotted as a function of the solar wind-to-magnetosphere time lag. For southward IMF (first panel), the reconnection driver vB_z (dashed curve) has a higher correlation coefficient with AE than does the eddy-viscosity driver; hence for southward IMF more of the variability of AE is controlled by vB_z. For northward IMF (second panel) the eddy-viscous driver (solid curve) has a higher correlation with AE than does vB_z; hence for northward IMF the eddy-viscous driver controls more of the variability of AE than does reconnection. Note in comparing the two panels of Figure 11 that the maximum correlation coefficients are similar (45.5% for eddy viscosity under northward IMF and 47.8% for vB_z under southward IMF), i.e., the eddy-viscosity driver drives about the same fraction of the variation of AE under northward IMF as vB_z drives under southward IMF [e.g., section 11.5 of *Freund*, 1981].

[33] For the other geomagnetic activity indices, the linear-correlation coefficients with $F_{\rm visc}$ for northward IMF are listed in Table 7. The correlations are performed both with and without a 1-hour time lag between the solar wind parameters and the geomagnetic indices. As can be seen in the table, in most cases the 1-hour time lag improves the correlation coefficients. The exceptions are the Dst index, which has a poor correlation in general, and the polar cap index PCI. Perhaps PCI responds more instantaneously to the viscous driver than do magnetospheric indices such as AE, AL, and AU.

[34] Multivariate linear-regression fits to the AE index AE = AE(vB_z, $F_{\rm visc}$) yield correlation coefficients higher than those of the AE = AE(vB,δB_{yz}) linear-regression fits (expressions (5) and (6)). This is particularly true if time lags between the solar wind and the magnetospheric indices are used. For a 1-hour time lag between AE and all solar wind parameters (which is optimal, as indicated by the plots in Figure 11), multivariate linear regression fits of the AE index as functions of vB_z and $nv^{5/2}(\delta B_{yz}/B)$ (which is proportional to $F_{\rm visc}$) are performed. The best fit for northward IMF (1000 nT km/s < vB_z < 3000 nT km/s) is

$$\mathrm{AE} = -0.0101vB_z + 2.96 \times 10^{-8}nv^{5/2}\left(\delta B_{yz}/B\right) + 77.1, \quad (15)$$

with a linear correlation coefficient $r_{\rm corr}$ of 46.5%. In expression (15) AE is in nT, vB_z is in nT km/s, n is in cm^{-3}, v is in km/s, and $\delta B_{yz}/B$ is dimensionless. The linear-correlation coefficient for the bivariate fit AE-vB_z is 4.7%

Table 7. Linear Cross-Correlation Coefficients r_{corr} (In Percent) Between vB_z and F_{visc} and F_{visc} With a 1-Hour Time Lag (Columns) and the Various Geomagnetic Activity Indices (Rows) for Northward Interplanetary Magnetic Field (IMF) (1000 nT km/s < vB_z < 3000 nT km/s)[a]

	vB_z No Lag	$nv^{5/2}(\delta B_{yz}/B)$ No Lag	$nv^{5/2}(\delta B_{yz}/B)$ 1-Hour Lag
AE	−3.5	+39.4	+45.5
AL	+3.1	−32.9	−37.1
AU	−3.2	+42.3	+46.5
Kp	+10.6	+50.5	+50.2
Dst	−8.2	−10.7	−10.6
ap	+10.4	+54.5	+53.2
PCI	−8.5	+36.3	+30.0

[a]One thousand six hundred sixty-four points go into each correlation, and the 95% confidence level of correlation is ±5.0%.

and for the bivariate fit AE-$nv^{5/2}(\delta B_{yz}/B)$ it is 45.5%. For southward IMF (1000 nT km/s < $-vB_z$ < 3000 nT km/s) the best fit is

$$\mathrm{AE} = -0.179 vB_z + 1.89 \times 10^{-8} nv^{5/2}\left(\delta B_{yz}/B\right) + 117.9, \quad (16)$$

with a linear-correlation coefficient r_{corr} of 54.0%. Again, AE is in nT, vB_z is in nT km/s, n is in cm^{-3}, v is in km/s, and $\delta B_{yz}/B$ is dimensionless. The linear-correlation coefficient for the bivariate fit AE-vB_z is 52.2% and for the bivariate fit AE-$nv^{5/2}(\delta B_{yz}/B)$ it is 15.5%. Note in expressions (15) and (16) that the coefficients between AE and $nv^{5/2}(\delta B_{yz}/B$ are similar (2.96×10^{-8} and 1.89×10^{-8}), indicating that the viscous driver operates with similar strength under northward and southward IMF.

6. Summary, Discussion, and Future Work

[35] The amplitude of the turbulence in the solar wind upstream of the Earth has a definite effect on the Earth's geomagnetic indices. Geomagnetic activity increases with an increase in the amplitude of the turbulence. This turbulence effect is present for both northward and southward IMF, but is more easily discerned for northward IMF.

[36] The interpretation of the results of sections 4 and 5 is that there is an eddy-viscous interaction between the solar wind and the magnetosphere that is controlled by the level of turbulence in the upstream solar wind. Louder upstream turbulence leads to a larger eddy viscosity (which is a larger Reynolds stress), which leads to more momentum transport from the solar wind flow into the magnetosphere, which leads to greater convection in the magnetosphere, which drives stronger current systems between the magnetosphere and the ionosphere, and which leads to elevated geomagnetic indices.

[37] Deriving an expression for the eddy-viscous stress force on the magnetosphere leads to a combination of solar wind parameters ($n^1 v^{5/2}(\delta B/B)^1$) that produces a correlation coefficient with AE that is larger than that obtained with the turbulence amplitude alone.

[38] For the data sets used, linear-correlation coefficients in the range 0.2–0.5 (cf. Tables 3, 6, and 7 and Figures 5, 9, 10, and 11) are found. Substantially improved correlation coefficients can be obtained from this same data set if solar wind values plus their time lags are used in the correlations. For instance, defining the shorthand notation $f_{visc} = n^1 v^{5/2}(\delta B_{yz}/B)^1$, the four-parameter linear-regression fit of AE(t) as a function of the simultaneous solar wind quantities $vB_z(t)$ and $f_{visc}(t)$ and the 1-hour time-lagged values $vB_z(t - \Delta t)$ and $f_{visc}(t - \Delta t)$ finds, for southward IMF,

$$\mathrm{AE}(t) = -0.0922 vB_z(t) + 2.42 \times 10^{-8} f_{visc}(t) - 0.0929 vB_z(t-\Delta t) + 9.36 \times 10^{-9} f_{visc}(t-\Delta t) + 115.9, \quad (17)$$

with a linear-correlation coefficient r_{corr} = 0.69, and, for northward IMF,

$$\mathrm{AE}(t) = 0.0214 vB_z(t) + 2.43 \times 10^{-8} f_{visc}(t) - 0.0484 vB_z(t-\Delta t) + 1.19 \times 10^{-8} f_{visc}(t-\Delta t) + 115.9, \quad (18)$$

with a linear-correlation coefficient r_{corr} = 0.68. These are significantly improved correlation coefficients over those corresponding to expressions (15) and (16). Note again that the coefficients of f_{visc} are nearly the same for southward IMF (expression (17)) and for northward IMF (expression (18)).

[39] The viscous interaction between the solar wind and the magnetosphere is often thought to be owed to instabilities on the boundary of the magnetosphere [*Eviatar and Wolf*, 1968; *Haerendel*, 1978], particularly Kelvin-Helmholtz type instabilities driven by the solar wind flow [*Mishin*, 1981; *Nykyri and Otto*, 2001]. In fluid interactions such as wind driving at the air-sea interface, the presence of turbulence in the wind leads to an enhanced surface drag and momentum coupling between the fluids [*Belcher et al.*, 1993; *Makin et al.*, 1995] and to enhanced driving of boundary layer waves [*Jeffreys*, 1925; *Miles*, 1993] including those of the Kelvin-Helmholtz type [*Cohen and Belcher*, 1999]. The addition of freestream turbulence in fluid flows can destabilize boundary layers [*Duck et al.*, 1996; *Wu*, 1999], changing the nature of fluid coupling to obstacles. For high Reynolds number MHD fluid flows, it would be remarkable if the presence of turbulence did not have these, plus other, effects.

[40] A rough estimate of the eddy viscosity of the magnetosheath flow can be made and compared with values in the literature of the viscosity believed to be necessary for the viscous interaction to operate. Including both the velocity fluctuation and the magnetic field fluctuation pieces, the MHD eddy viscosity is $\nu_{eddy} = C_\nu K^2/\varepsilon$ (e.g., equation (24) of *Yoshizawa and Yokoi* [1996]) where $K = 0.5(\delta u^2 + \delta B^2/4\pi n m_i)$ (e.g., equation (20) of *Yoshizawa and Yokoi* [1996]) is the turbulent energy per unit mass and where $\varepsilon = \partial K/\partial t$ (e.g., equation (26) of *Yoshizawa* [1990]) is the dissipation rate of turbulent energy. Taking $\varepsilon = K/\tau_{auto}$ (e.g., equation (1.5.13) of *Tennekes and Lumley* [1972]), where τ_{auto} is the autocorrelation time of the turbulence (= the eddy turnover time), the MHD eddy viscosity is

$$\nu_{eddy} = C_\nu 0.5\left(\delta u^2 + \delta B^2/4\pi n m_i\right)/\tau_{auto}. \quad (19)$$

Taking C_ν = 0.06 (from section 5), δv = 40 km/s (from Table 2), δB = 12 nT (from Table 3 of Borovsky and Funsten, 2003), n = 25/cm (from Table 3 of *Borovsky and Funsten* [2003]), and τ_{auto} = 30 s (from an examination of ISE E-2 Fast Plasma Experiment data), expression (3) yields $\nu_{eddy} = 3.9 \times 10^{13}$ cm^2/s for the eddy viscosity of the magnetosheath. Note that this value will vary from day to day as the level of turbulence in the magnetosheath changes. Arguments in the literature for what size of viscosity is needed to produce boundary layers on the magnetosphere of a given thickness yield viscosity estimates of 10^{13} cm^2/s [*Axford*, 1964], 10^{14} cm^2/s [*Mishin*, 1979], and 10^{13} cm^2/s [*Sonnerup*, 1980]. As can be seen, the value of the eddy viscosity of the turbulent magnetosheath is in the range of the estimates of the viscosity needed to produce the viscous interaction. The eddy viscosity of the magnetosheath can be compared with estimates of diffusion coefficients obtained from observations of particle diffusion at the magnetopause [*Reiff et al.*, 1977; *Sckopke et al.*, 1981] by first relating the eddy viscosity ν_{eddy} to an eddy diffusion coefficient D_{eddy} and then writing the diffusion coefficient in the form of a Bohm diffusion coefficient. The turbulent Schmidt number $Sc_t = \nu_{eddy}/D_{eddy}$ is the ratio of the eddy viscosity ν_{eddy} to the eddy diffusion coefficient D_{eddy}. The turbulent Schmidt number typically is $Sc_t \approx 0.6$ [*Antoine et al.*, 2001; *Flesch et al.*, 2002], but may deviate from this value near a boundary (e.g., Figure 3 of *Koeltzsch* [2000], and see also Figure 11 of *Smolentsev et al.* [2002]). For $Sc_t = 0.6$, $D_{eddy} = 1.66\nu_{eddy}$. For $\nu_{eddy} = 3.9 \times 10^{13}$ cm^2/s, this gives $D_{eddy} = 6.6 \times 10^{13}$ cm^2/s. This value of D_{eddy} is in the range of the estimate $D = 10^{13}$ cm^2/s given by *Sckopke et al.* [1981] to produce the observed thickness of the boundary layer. The Bohm diffusion coefficient $D_B = \alpha c k_B T/eB$, where $\alpha = 1/16$ for classical Bohm diffusion [see section 1.14 of *Krall and Trivelpiece*, 1973]. Writing the eddy diffusion coefficient D_{eddy} in the form of the Bohm diffusion coefficient as did Reiff et al. yields $D_{eddy} = \alpha c k_B T/eB$. Using the above value of $D_{eddy} \approx 6.6 \times 10^{13}$ cm^2/s and using $T_i \approx 400$ eV, and $B \approx 25$ nT for the magnetosheath (Table 3 of *Borovsky and Funsten* [2003]), this expression yields $\alpha \approx 0.41$. Note again that this value will vary from day to day as the level of turbulence in the magnetosheath varies. This value is similar to the value $\alpha = 1.2$ that Reiff et al. obtained by fitting the dispersion profiles of particles diffusing at the magnetopause. So again, the value of the eddy viscosity of the magnetosheath is in the range required to produce the viscous interaction.

[41] The results of this work compare favorably with an assessment of the efficiency of the viscous interaction for powering the magnetosphere [*Tsurutani and Gonzalez*, 1995]. That assessment was made by looking at the strength of the AE index during a set of strongly northward-IMF events. Extracting the events listed in Table 1 of Tsurutani and Gonzalez from our large data set (but removing 2 hours of that data that had southward B_z GSM) and performing the δB_{yz} versus AE correlation for those event times, a 46.6% correlation coefficient is found, where the 95% confidence level is at 32.9%. The slopes and intercepts of the linear regression for the Tsurutani and Gonzalez events are very similar to the slopes and intercepts for the full 3 years of data, meaning that these events fit in with the general trend of turbulence in the solar wind producing elevated geomagnetic activity, i.e., the events are not special. For the purpose of discussion, Tsurutani and Gonzalez make the assumption that the viscous coupling is about 10% as efficient as is reconnection; from Table 5 of the present paper one would argue that it is about 20% as efficient for powering the currents that are measured by the AE index. Among their various events, Tsurutani and Gonzalez find a variability in the viscous-interaction efficiency which they cannot account for; this paper has uncovered a reason for such variability: control of the viscous interaction by the amplitude of solar wind turbulence.

[42] Note that the correlation between the amplitude of the solar wind turbulence and the level of geomagnetic activity discussed in this report differs from the effects emphasized for HILDCAA events [*Tsurutani and Gonzalez*, 1987; *Tsurutani et al.*, 1995], where large amplitude, very low frequency Alfven waves in the solar wind cause the IMF to swing southward and become geomagnetically effective. In section 4, such a B_z-reversal effect was investigated as an explanation of the turbulence effect under northward IMF and the turbulence effect was found to persist when B_z reversals were eliminated. The periods most relevant to HILDCAA events are hours; the periods of most relevance for the eddy viscosity effect are in the range of less than a minute to a few minutes.

[43] Computer simulations verify what has been known for over a century, namely that turbulence has affects on nearly every aspect of fluid dynamics [e.g., sections 365–369 of *Lamb*, 1932]. But a computer simulation of a flow does not allow turbulence and does not capture the effects of turbulence correctly unless numerical dissipation in the simulation is low and unless spatial resolution in the simulation is high (i.e., the simulation code must have a sufficiently high Reynolds number). In MHD simulation of the solar-wind-driven magnetosphere, the computer codes that are used have advanced to the point of just seeing the larger-scale fluctuations of MHD turbulence in the magnetosphere [e.g., *White et al.*, 2001; *Sonnerup et al.*, 2001], but they have not yet advanced sufficiently to see turbulence in the solar wind or magnetosheath. To get turbulence and its effects correct in numerical simulations, the simulation codes must either (1) fully resolve the flow from large scales down to the dissipation scale of the turbulence with a so-called direct numerical simulation (DNS) or (2) turbulence must be accounted for by inclusion of a turbulence model into the codes where the turbulence model predicts how and where turbulence evolves in the flow and calculates the feedback of the turbulence on the flow. For space plasmas, resolving MHD turbulence down to the dissipation scale requires grid resolution below the ion gyroradius or below the ion inertial length. For global magnetospheric simulations this resolution requirement makes DNS impractical at present. There are two easier options for computation beside DNS [cf. *Spalart*, 2000; part two of *Pope*, 2000; section 5.1 and chap. 8 of *Mathieu and Scott*, 2000]. The first is large eddy simulation (LES), wherein the larger-scale fluctuations of the turbulence are resolved by the computational grid of a medium Reynolds number simulation code and the effects of the smaller-scale portions of the turbulence are emulated with transport coefficients calculated from a turbulence model [*Theobalk et al.*, 1994; *Agullo et al.*, 2001]. The second option is Reynolds averaged Navier Stokes (RANS) or Reynolds averaged MHD, wherein only the nonfluctuating mean flow is resolved by a low Reynolds number simulation code and the effects of turbulence are put in with transport coefficients calculated from a turbulence model [*Kenjeres and Hanjalic*, 2000; *Hanjalic and Ken-*

jeres, 2001]. When a turbulence model is used in a simulation to represent the affects of turbulence with transport coefficients, the most important coefficient is eddy viscosity, which is an approximation to the Reynolds stress [e.g., *Okamoto*, 1994; *Gatski and Jongen*, 2000]. This viscosity represents the greatly enhanced momentum transport owed to turbulent fluctuations. Whereas a large kinematic (molecular) viscosity will act to suppress turbulence, the eddy viscosity represents the action of turbulence. Introduction of a large eddy viscosity will lower the effective Reynolds number of a simulation, but not in the sense that the lower Reynolds number situation will be absent of turbulence. Rather on the contrary, eddy viscosity signifies rather than suppresses turbulence. In low Reynolds number MHD codes used for global magnetospheric simulations, numerical diffusivity and numerical resistivity which are inherent in the codes can emulate eddy viscosity and eddy resistivity [cf. *Porter and Woodward*, 1994; *Cottet*, 1996], but without control of the magnitude of the eddy viscosity and without the proper parametric dependences (i.e., on the time history of the fluid shear). Because direct numerical simulations of everyday large Reynolds number flow problems (e.g., aircraft, automobiles, submarines, and buildings) are so impractical, there is a vast research effort in fluid dynamics aimed at improving turbulence models for incorporation into LES and RANS simulation codes [*Rodi*, 1997; *Henkes*, 1998; *Speziale*, 1998; *Murakami*, 1998]. For space physics, it should be pondered whether such an effort is needed to improve MHD simulations of the solar wind driven magnetosphere. On one hand, the phenomenological consequences of turbulence for solar system flows have not been well established and there are no wind-tunnel experiments where dials can be turned to aid in the construction of MHD turbulence models. On the other hand, there is the hard-earned lesson of fluid dynamics: If getting the right answer matters, turbulence, if present, must be accounted for.

[44] Accounting for eddy-viscosity effects in the coupling of the solar wind to the Earth's magnetosphere can lead to a fuller understanding of how the magnetosphere is driven and can lead to more accuracy in the prediction of geomagnetic activity and so-called space weather. Measuring the influence that solar wind turbulence has on the magnetosphere is one of the few ways that plasma researchers can use to study the dynamical effects of turbulence in MHD flows and the coupling of large-scale plasmas at high Reynolds numbers. The turbulent solar wind interacting with the Earth's magnetosphere provides a test case to discern which turbulent-viscosity effects play roles for astrophysical plasma flows [e.g., *Armitage*, 1998; *Balbus and Hawley*, 1998].

[45] To enhance our understanding of this turbulence effect, more work needs to be done. (1) A two-satellite study is needed to obtain a parameterization of the levels of MHD turbulence in the magnetosheath in terms of the level of MHD turbulence in the upstream solar wind. With such a parameterization, a more accurate eddy diffusion coefficient at the Earth can be derived in terms of the upstream solar wind parameters. (2) High time resolution solar wind data should be used to construct a measure of the solar wind turbulence with a time resolution of about a few minutes, and a scheme should be developed to remove rotational/tangential discontinuities from the turbulence measures. With these cleaner, higher time resolution measurements of the solar wind turbulence, improved correlations for the turbulence effect should be expected. (3) A statistical analysis of satellite flow measurements should be used to search for evidence of momentum loss in the magnetosheath plasma flow adjacent to the magnetopause. If there is any viscous interaction between the magnetosheath and the magnetosphere, then, close to the magnetosphere, there should be velocity gradients (rates of strain) that correspond to the viscous shear stresses [see section 1.1 of *Young*, 1989]. Such evidence of magnetosheath momentum loss would confirm and allow improvement of the fluid boundary layer approximation used to calculate the total eddy-viscous force of the solar wind flow on the magnetosphere. (4) The nature of the turbulence in the magnetosheath near the magnetopause needs to be characterized (correlations among the fluctuation-velocity components, nature of magnetic field and velocity spectra, anisotropies, etc.) in order to obtain improved values for the eddy viscosity and the turbulent resistivity.

Appendix A: Autocorrelation Functions of Solar Wind Quantities

[46] In this appendix, the autocorrelation functions and autocorrelation times of pertinent solar wind quantities are examined. For a time series $f(t)$, the autocorrelation function $A(\Delta t)$ of f is defined as

$$A(\Delta t) = \int [f(t) - \langle f \rangle][f(t+\Delta t) - \langle f \rangle]dt/A(0), \qquad \text{(A1)}$$

with

$$A(0) = \int [f(t) - \langle f \rangle][f(t) - \langle f \rangle]dt, \qquad \text{(A2)}$$

where Δt is the time shift between the time series of data and itself, and $\langle f \rangle$ is the average value of f.

[47] In Figure 12, the autocorrelation functions of vB_z, $|B|$, δB_{yz}, and $\delta B_{yz}/B$ are plotted. The autocorrelation time (using the $1/e$ method) for vB_z is $\sim$5 hours and for $|B|$ it is $\sim$14 hours. The $\sim$5-hour autocorrelation time of vB_z is similar to the $\sim$6-hour cross-correlation time between vB_z and AE (see Figure 11) and may be the origin of that cross-correlation time. In Figure 12, δB_{yz} and $\delta B_{yz}/B$ have two-component autocorrelation functions. The fast components have autocorrelation times of $\sim$1 hour (for hourly averaged data) and the slow components have autocorrelation times of $\sim$9 hours for δB_{yz} and $\sim$7 hours for $\delta B_{yz}/B$. These slower autocorrelation times are similar to the cross-correlation times seen between δB_{yz} and the various geomagnetic activity indices (cf. Figure 9) and between $\delta B_{yz}/B$ and the various indices (cf. Figure 10).

[48] In Figure 13, higher time resolution data is used to construct the autocorrelation function of δB_{yz} in the solar wind. The curve with solid points is the autocorrelation function of δB_{yz} constructed with 3 years of 1-hour-resolution OMNI data. The curve without points is the autocorrelation function of δB_{vec} constructed with 27 days of 4-min-averaged values from the ACE data set. Here δB_{vec} is

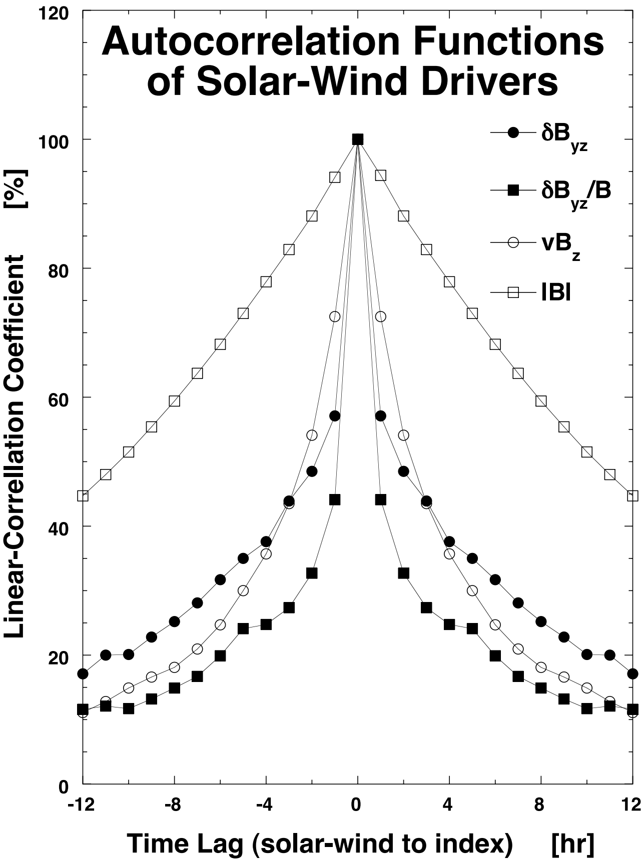

Figure 12. The autocorrelation functions for the various solar wind quantities that drive the magnetosphere. Exponential fits $\exp(-t/t_{corr})$ yield autocorrelation times t_{corr} of $\sim$14 hours for $|B|$ and $\sim$5 hours for vB_z. The autocorrelation function for δB_{yz} has a component with a rapid falloff followed by a component with an autocorrelation time of $\sim$9 hours and $\delta B_{yz}/B$ has a rapid falloff followed by a component with an autocorrelation time of $\sim$7 hours.

the standard deviation of 0.33-s time resolution measurements of the vector magnetic field

$$\delta B_{vec} = \left[\left\langle (B_x - \langle B_x\rangle)^2\right\rangle + \left\langle \left(B_y - \left\langle B_y\right\rangle\right)^2\right\rangle + \left\langle (B_z - \langle B_z\rangle)^2\right\rangle\right]^{1/2} \tag{A3}$$

(C. Smith, private communication, 2002). Note that in the higher time resolution solar wind data, the fast component of the autocorrelation function is even faster, $\sim$4 min for the 4-min ACE data.

[49] Rotational/tangential discontinuities are ubiquitous in the solar wind [*Neugebauer and Alexander*, 1991; *Tsurutani and Ho*, 1999]. Each discontinuity produces a burst of δB_{yz} that is uncorrelated with surrounding temporal values of δB_{yz}. This leads to a fast decay in the autocorrelation function. It seems likely that the fast components of the autocorrelation functions of δB_{yz} and $\delta B_{yz}/B$ are owed to the presence of rotational/tangential discontinuities in the solar wind, rather than a bursty nature of the level of turbulence in the solar wind. If the contribution to δB_{yz} owed to rotational/tangential discontinuities could be removed, the cross correlations between δB_{yz} and the various geomagnetic activity indices probably could be improved.

Appendix B: Significance of the Correlations

[50] In sections 4 and 5, correlations between the values of various driver functions in the solar wind and the values of various geomagnetic indices were explored, with the degree of correlation indicated by a linear correlation coefficient r_{corr}. The rule of thumb $r_{corr} > 2/N^{1/2}$ was used to determine whether a correlation between two quantities was significant or not. As discussed below, this rule of thumb strictly applies only to data that have Gaussian (normal) distributions. As will be seen below, the distributions of the values of the various solar wind drivers and the various geomagnetic indices are not Gaussians. Therefore the validity of the correlations indicated by the correlation coefficients r_{corr} are further explored.

[51] In Figures 14–16, the occurrence distributions of various quantities used in this solar wind/magnetosphere coupling study are shown. In Figure 14, the occurrence distribution of hourly averaged values of the solar wind quantities vB_z (first panel) and $|B|$ (second panel) for 1979–1981 are shown. In Figure 15, the occurrence distribution of hourly averaged values of the solar wind turbulence quantities δB_{yz} (first panel), $\delta B_{yz}/B$ (second panel), and $nv^{5/2}$ ($\delta B_{yz}/B$) (third panel) for 1979–1981 are shown. As can be seen in the various panels of these two figures, none of the occurrence distributions of solar wind driver values are Gaussian.

[52] In Figure 16, the occurrence distributions of the hourly averaged values of the auroral-electrojet index AE (first panel), the hourly averaged values of the auroral-electrojet indices AL and AU (second panel), 3-hour-averaged values of the Kp index (third panel), hourly averaged values of the polar cap index PCI (fourth panel), and hourly averaged values of the Dst index (fifth panel) are plotted, all for 1979–1981. As can be seen in this figure, none of the distributions of geomagnetic-index values are Gaussian.

[53] For N data points (x,y), the correlation coefficient r_{corr} between x and y is calculated with

$$r_{corr} = \Sigma(X_i Y_i)/\left[\left(\Sigma X_i^2\right)\left(\Sigma Y_i^2\right)\right]^{1/2} \tag{B1}$$

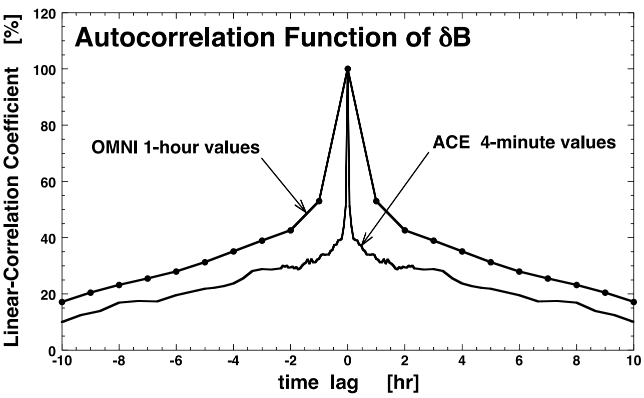

Figure 13. The autocorrelation function of the turbulence amplitude in the solar wind with 1-hour time resolution and with 4-min time resolution.

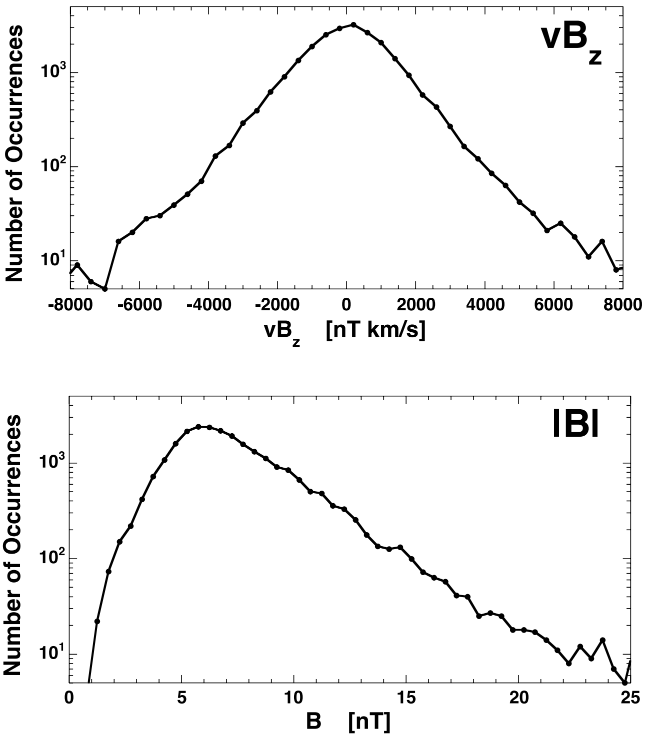

Figure 14. The occurrence distribution of hourly averaged values of vB_z (first panel) and $|B|$ (second panel) in the solar wind in 1979–1981.

[e.g., section 11.2 of *Bevington and Robinson*, 1992] where $X_i = (x_i - x_{ave})$ and $Y_i = (y_i - y_{ave})$, with x_{ave} being the average of the N values of x and y_{ave} being the average of the N values of y, and where all sums Σ are performed from $i = 1$ to $i = N$. For N data points (x,y) that have a bivariate normal distribution $g(x,y,\rho) = \exp\{-(x^2 - 2\rho xy + y^2)/(2[1 - \rho^2])\}$ (e.g., equation (26.3.1) of *Abramowitz and Stegun* [1964]), the statistical significance of a correlation coefficient can be judged with the rule of thumb that the two variables x and y are definitely correlated if the correlation coefficient $r_{corr} > 2/N^{1/2}$. This rule of thumb comes from the fact that, for bivariate normal data with no correlation ($\rho = 0$), the distribution of correlation coefficients r_{corr} is a Gaussian with mean of 0 and a standard deviation $\sigma = (N - 1)^{-1/2}$, where N is the number of data points [see section 19.12 of *Hald*, 1952]. Since 5% of the area under a Gaussian distribution lies beyond 1.64σ, the 95% confidence level for correlation occurs for $r_{corr} > 1.64\sigma$, which is $r_{corr} > 1.64/(N - 1)^{1/2}$. For large N this is approximately $r_{corr} > 2/N^{1/2}$. If the distribution of data points (x,y) is a bivariate normal distribution $g(x,y,\rho)$, then the distribution of x values is a Gaussian (normal distribution) and the distribution of y values is a Gaussian. This can be seen by integrating the bivariate normal distribution $g(x,y,\rho)$ over either x or y.

[54] Since none of the distributions of values used in this study are Gaussian (see Figures 14–16), none of the sets of data points (x,y) used in the correlations are bivariate normal distributions. Hence the rule of thumb used to determine whether or not a correlation is significant must be questioned. For the statistics of the solar wind drivers and geomagnetic indices, which are not Gaussian, the significance of the correlation coefficient is double checked with the following statistical analysis. To determine what magnitude of correlation coefficient r_{corr} is consistent with no correlation, the data sets are repeatedly randomized and the correlation coefficient is calculated each time. Then a distribution function of correlation coefficients for the random data is constructed and the correlation in question is compared with this distribution. Here randomizing a data set of N points (x,y) means randomizing the x values and randomizing the y values and repairing the x values with y values into N points (x,y). The solar wind driver value is x and y is a geomagnetic-index value. The results of three of these tests are shown in the three panels of Figure 17: δB_{yz} versus AE (first panel), $\delta B_{yz}/B$ versus AE (second panel), and F_v versus AE (third panel). For all three of these cases $N = 1664$. For each case the randomization process was repeated 10,000 times to yield 10,000 r_{corr} values. In each of the three panels, the value of the correlation coefficient

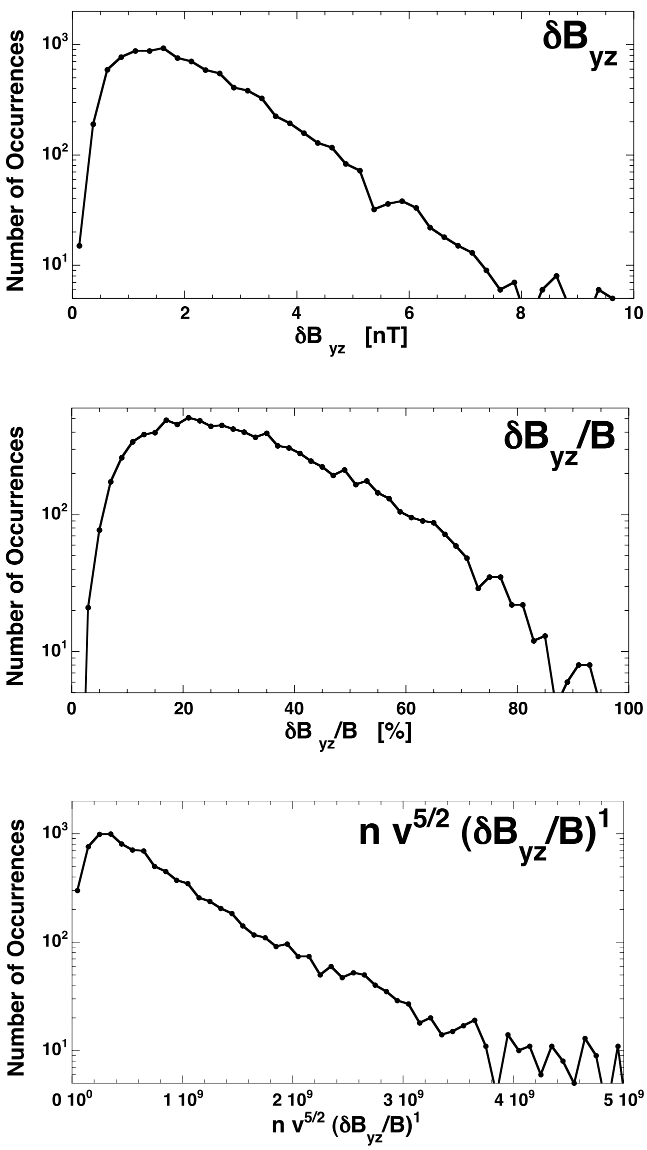

Figure 15. The occurrence distribution of hourly averaged values of δB_{yz} (first panel), $\delta B_{yz}/B$ (second panel), and $nv^{5/2}$ $(\delta B_{yz}/B)$ (third panel) in the solar wind in 1979–1981.

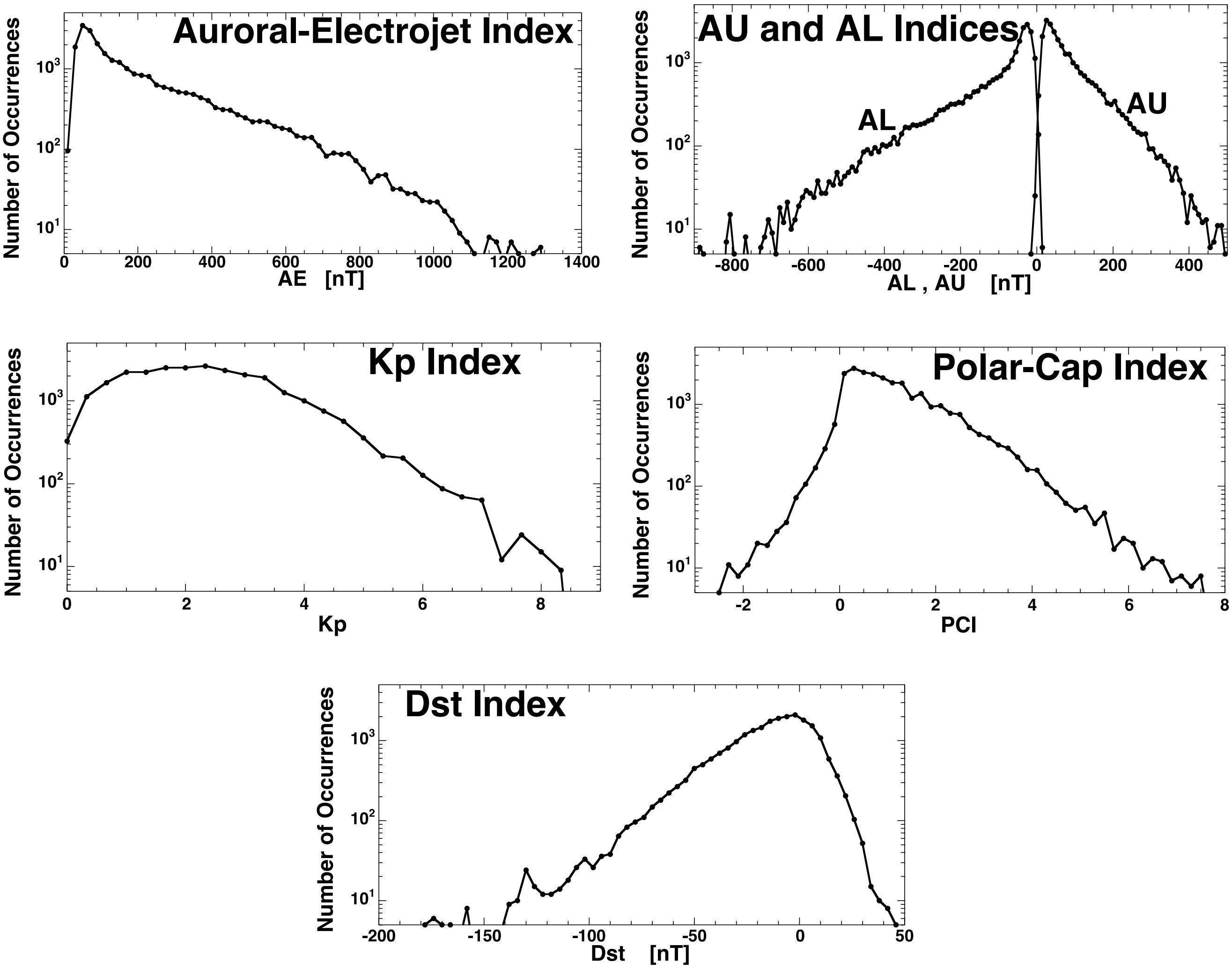

Figure 16. The occurrence distributions of various geomagnetic indices during 1979–1981: hourly averaged AE (first), hourly averaged AU and AL (second), 3-hour-averaged Kp (third), hourly averaged PCI (fourth), and hourly averaged Dst (fourth).

obtained for the nonrandomized data is indicated with a bar. For all three cases the correlation value in question lies far outside the distribution of noncorrelated data. For δB_{yz} versus AE, the standard deviation of the random-data r_{corr} values is 2.44% and r_{corr} is 33.6%; for δB_{yz} versus AE, the standard deviation of the random data r_{corr} values is 2.41% and r_{corr} is 23.9%: and for F_v versus AE, the standard deviation of the random-data r_{corr} values is 2.50% and r_{corr} is 39.4%. The distributions of r_{corr} values appear to be Gaussian and the standard deviations are all approximately $(N - 1)^{-1/2}$, which is 2.45% for $N = 1664$ data points. Hence the fact that the data are not a bivariate normal population does not appear to invalidate the rule of thumb that correlation is definite for $r_{\mathrm{corr}} > 2/N^{1/2}$. For δB_{yz} versus AE the correlation is at the 13.8σ level, for $\delta B_{yz}/B$ versus AE the correlation is at the 9.9σ level, and for F_v versus AE the correlation is at the 15.8σ level. Correlation at the 2σ level (= 97.7% confidence level) is significant.

[55] Two conclusions are drawn. (1) The correlations found in sections 4 and 5 between the level of turbulence and the geomagnetic indices are definite and are inconsistent with random correlation coefficients for the data. (2) The rule of thumb that is used in the body of this report (that correlation at the 95% confidence level occurs for $r_{\mathrm{corr}} > 2/N^{1/2}$) holds, with $2/N^{1/2}$ approximating the 2σ level. With 1664 data points (appropriate for all three cases tested explored here), $2/N^{1/2} = 4.9\%$.

Appendix C: Viscous Drag on the Magnetosphere

[56] In this Appendix, the coefficient of viscous drag C_{visc} (see expression (8)) for a magnetosphere-shaped obstacle in a flow is derived as a function of the Reynolds number of the flow past the obstacle. The magnetospheric obstacle is taken to be a hemisphere of radius r followed by a cylinder of radius r and length h (see Figure 18). To get the coefficient of viscous drag C_{visc}, the viscous drag force F_{visc} (which is the local viscous shear stress integrated over the entire surface of the magnetosphere) will be calculated. This will be done by computationally determining the structure of a viscous boundary layer that forms on a magnetosphere-shaped obstacle in a flow. For ordinary

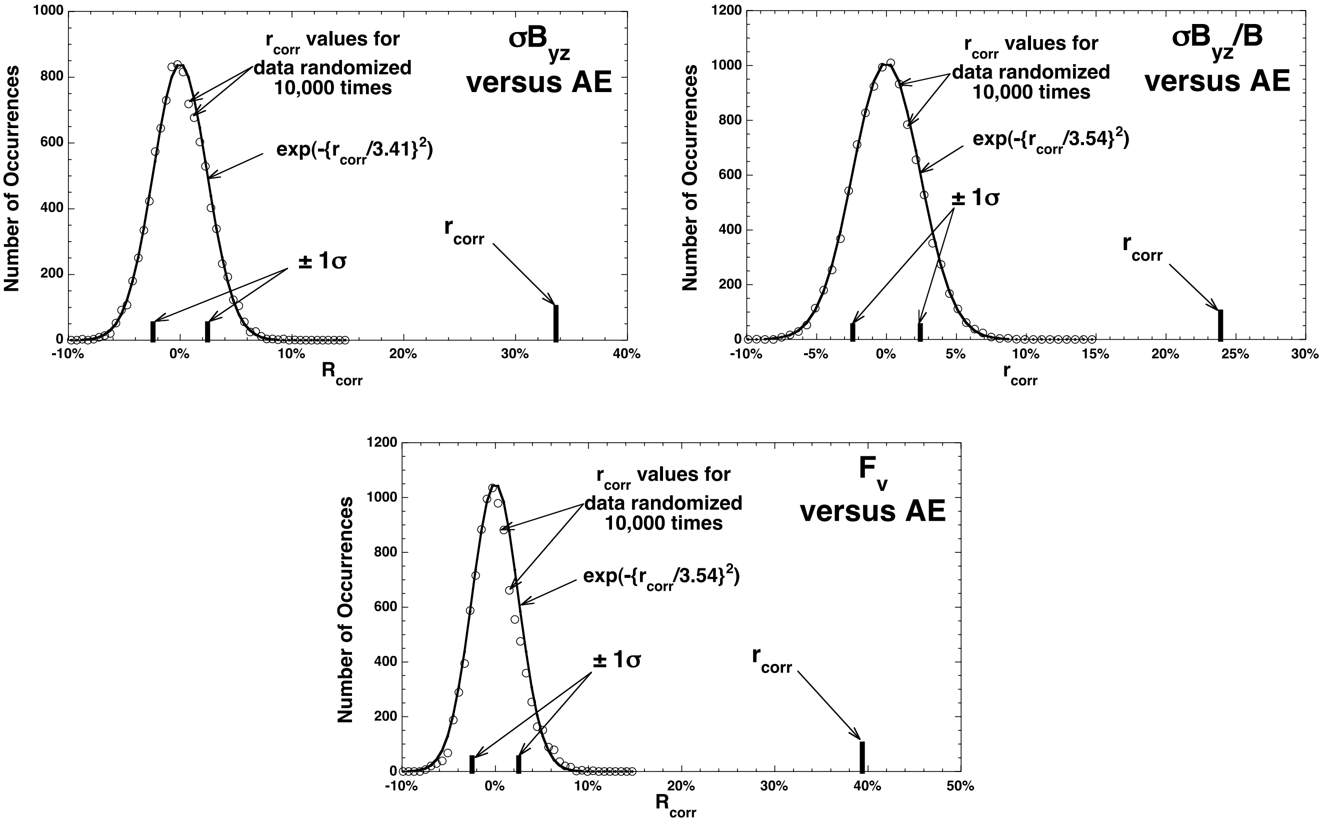

Figure 17. By repeatedly randomizing the data in the data sets and calculating the correlation coefficients, distributions of correlation coefficients for random (uncorrelated) data are constructed (points). The correlation coefficients for the unrandomized data (bars) are compared with these distributions. The first panel pertains to δB_{yz} versus AE, the second panel pertains to $\delta B_{yz}/B$ versus AE, and the third panel pertains to $nv^{5/2}(\delta B_{yz}/B)$ versus AE.

Navier-Stokes fluids, the viscous boundary layer has a thickness that scales as $Re^{-1/2}$, where Re is the ordinary Reynolds number. For MHD flows, as long as magnetic field lines do not cross the surface of the obstacle from the obstacle into the flow (in which case a Hartmann layer results [see section 5.10 of *Shercliff*, 1965 and see section 10.4 of *Jackson*, 1975]), MHD effects are minor and an ordinary viscous boundary layer that scales as $Re^{-1/2}$ results [e.g., *Sears*, 1961; see sections 12.5.2 and 12.6 of *Sutton*, 1965; see section 12.6 of *Hughes and Young*, 1966], as is the case for a Navier-Stokes fluid.

[57] If u_∞ is the flow upstream of the hemisphere, the Reynolds number Re of the flow will be given by expression (9): $Re = u_\infty d/\nu_{\mathrm{kin}} = u_\infty 2r/\nu_{\mathrm{kin}}$, where d and r are the diameter and radius of the hemisphere (magnetosphere) and ν_{kin} is the kinematic viscosity of the fluid. (Note, in this appendix u is chosen for velocity rather the v to avoid confusion with viscosity ν.) Ordinarily for boundary layer theory, ν_{kin} is taken to be the molecular kinematic viscosity, but in section 5 a turbulent viscosity will be taken for ν_{kin}. A fluid flowing around an obstacle with a Reynolds number Re greater than about 20 will form a boundary layer on the obstacle [e.g., *Mathieu and Scott*, 2000]: outside the boundary layer the flow pattern is insensitive to the value of ν_{kin} and inside the boundary layer the value of ν_{kin} affects the flow. Taking x to be the direction tangential to the object's surface with x increasing downstream from the nose (see Figure 18) and y to be the direction normal to the surface, the notation u_{0x} is taken for the tangential flow velocity just outside the boundary layer, which is independent of the fluid viscosity and the boundary layer structure. This flow velocity u_{0x} as a function of x is (e.g., equation (11.38) and section VII.e of *Schlichting* [1979])

$$u_{0x}(x) = (3/2)u_\infty \sin(x/r) = (3/2)u_\infty \sin(\theta), \qquad \text{(C1)}$$

where u_∞ is the flow far from the hemisphere. Just outside of the boundary layer along the cylinder the tangential flow is

$$u_{0x}(x) = (3/2)u_\infty, \qquad \text{(C2)}$$

with a no-slip boundary condition, u_x will be zero everywhere at the surface of the obstacle. The viscous shear force τ per unit area on the obstacle (which is a shear stress generated at the expense of momentum lost by the fluid within the boundary layer) is given by (e.g., equation (7.24) of *Pope* [2000])

$$\tau = \nu_{\mathrm{kin}}\rho\partial u_x/\partial y \qquad \text{(C3)}$$

evaluated in the boundary layer at the surface of the obstacle, where ν_{kin} is the kinematic viscosity of the fluid, ρ is the mass density of the fluid, u_x is the flow velocity in the x direction (parallel to the surface), and $\partial/\partial y$ is the spatial derivative normal to the surface. The quantity $\partial u_x/\partial y$ is a

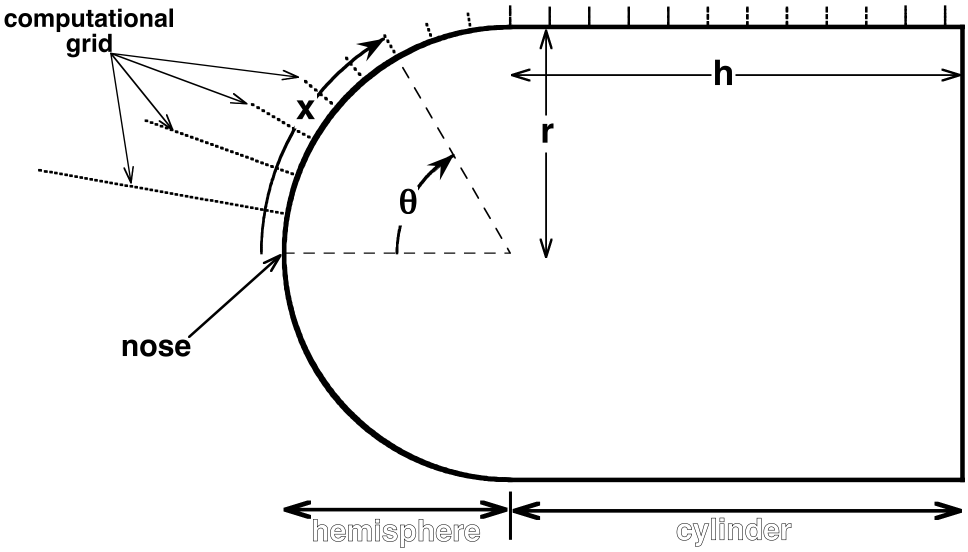

Figure 18. The shape taken for the magnetosphere for the purpose of calculating the total viscous force on it. Shown also is the convecting compressible computational grid.

velocity shear or rate of strain. The derivative $\partial u_x/\partial y$ needed for expression (C3) is estimated by computationally solving for the structure of the boundary layer along the obstacle. Within the boundary layer, viscous diffusion acts on the vorticity caused by the boundary condition of the obstacle, broadening the region of shear. The boundary layer is thinnest on the upstream end and grows in thickness toward the downstream end, with the growth in thickness owed to the progressive action of viscous diffusion as fluid flows downstream within the boundary layer. Viscous diffusion of velocity shear is described by

$$\partial u_x/\partial t = \nu_{\mathrm{kin}}\partial^2 u_x/\partial y^2 \qquad \text{(C4)}$$

(e.g., equations (4.3) and (4.7) of *Mathieu and Scott* [2000]). The partial differential equation (C4) is computationally solved for $u_x(y,t)$ on a one-dimensional grid in the y direction with appropriate boundary conditions. As time evolves, the grid is translated in the x direction along the obstacle with the tangential flow velocity and the grid is compressed in y (see Figure 18). These two processes are discussed in the following two paragraphs.

[58] The convection of the grid in the x direction is handled as follows. Across the boundary layer the fluid velocity u_x varies from $u_x = 0$ at the surface of the obstacle to $u_x = u_{0x}$ out in the unperturbed fluid. At a "midpoint" in the boundary layer, the fluid velocity is $(1/2)u_{0x}$. The convection velocity u_{grid} of the grid in the x direction is taken to be at $u_{\mathrm{grid}} = (1/2)u_{0x}$, which is the convection velocity associated with the midpoint of the diffusing gradient. As time t evolves, the grid moves in x, where x and t are related by

$$t = \int_0^x [(1/2)u_{0x}(x)]^{-1}dx. \qquad \text{(C5)}$$

With expressions (C1) and (C2), expression (C5) is

$$t(x) = (4/3u_\infty)\int_0^x [\sin(x/r),1]^{-1}dx, \qquad \text{(C6)}$$

where the quantity in the square bracket in the integrand is equal to $\sin(x/r)$ for $x \le (\pi/2)r$ (hemisphere) and is equal to 1 for $x \ge (\pi/2)r$ (cylinder). Note that there is a stagnation point in the flow at the nose of the magnetosphere at $\theta = x/r = 0$ (see expression (C1)). In the convection-time integral (C6) this stagnation leads to a logarithmic divergence at the $x = 0$ limit. In reality, diffusive transport will dominate convective transport in the vicinity of the stagnation point. This can be used to introduce a physical cutoff to the integral: within a region of radius a around the stagnation point, the convective velocity $(3/4)u_\infty\sin(\theta)$ will be replaced with a diffusive velocity u_{diff}. The values of a and u_{diff} are determined by defining a diffusive velocity from the diffusion equation in cylindrical coordinates, where, near $x = 0$, x represents a radial distance:

$$\partial f/\partial t = \nu_{\mathrm{kin}}\partial^2 f/\partial x^2 + \nu_{\mathrm{kin}}(1/x)\partial f/\partial x, \qquad \text{(C7)}$$

which yields a viscous diffusion timescale $t_{\mathrm{diff}} = a^2/2\nu_{\mathrm{kin}}$ for information to spread to a radius a. Defining an effective diffusion velocity $u_{\mathrm{diff}} = a/t_{\mathrm{diff}}$ in this region, and using $t_{\mathrm{diff}} = a^2/\nu_{\mathrm{kin}}$ gives

$$u_{\mathrm{diff}} = 2\nu_{\mathrm{kin}}/a. \qquad \text{(C8)}$$

Setting $u_{\mathrm{diff}} = (1/2)u_0(a)$ and using expressions (C6) and (C8) yields the expression

$$2\nu_{\mathrm{kin}}/a = (3/4)u_\infty \sin(a/r). \qquad \text{(C9)}$$

Using $\sin(a/r) \approx a/r$, this expression is solved for a to yield

$$a = r(8\nu_{\mathrm{kin}}/3u_\infty r)^{1/2} \qquad \text{(C10)}$$

for the cutoff value of x in the integral of expression (C6). Expression (C6) is rewritten as

$$t = \int_0^a [u_{\mathrm{diff}}]^{-1}dx + (4/3u_\infty)\int_x^a [\sin(x/r),1]^{-1}dx. \qquad \text{(C11)}$$

The first integral is equal to a/u_{diff}, which, using expression (C8) for u_{diff} and expression (C10) for a, is equal to $4r/3u_{\infty}$. Using a table of integrals, the second integral is performed and expression (C11) becomes

$$t = (4r/3u_{\infty})[\log_{\mathrm{e}} \tan(x/2r) + A_1], \tag{C12}$$

for $x \leq (\pi/2)r$ (hemisphere) or

$$t = (4r/3u_{\infty})[x/r + A_1 - \pi/2], \tag{C13}$$

for $x \geq (\pi/2)r$ (cylinder), where

$$A_1 = 1 + (1/2)\log_{\mathrm{e}}(3Re/4), \tag{C14}$$

where $\log_{\mathrm{e}} \tan(\varepsilon^{-1/2}) \approx -(1/2)\log_{\mathrm{e}}(\varepsilon)$ was used for $\varepsilon \ll 1$ and where expression (9) for the definition of the Reynolds number R was used. Expressions (C12) and (C13) can each be algebraically inverted to give the position x of the grid as a function of t:

$$x/r = 2\mathrm{inv}\tan\{\exp[(3u_{\infty}/4r)t - A_1]\}, \tag{C15}$$

for $x/r \leq \pi/2$ (hemisphere) and

$$x/r = (3u_{\infty}/4r)t - A_1 + \pi/2, \tag{C16}$$

for $x/r \geq \pi/2$ (cylinder).

[59] The compression of the grid in y is handled as follows. As the tangential velocity $u_{0x} = (3/2)u_{\infty} \sin(x/r)$ increases with x going from the nose of the hemisphere to the terminator, the streamlines of flow compress in the y direction (see, e.g., Figure 6.8.1 of *Batchelor* [1970]). This compression of the streamlines in y steepens y gradients and amplifies the shear $\partial u_x/\partial y$, which counteracts the diffusive spreading of u_x in y. As the computational grid is translated in x, it is contracted in y according to the contraction of the unperturbed streamlines. If the grid is started at x-position x_0 with an initial gridspacing Δy_0, then conservation of mass with tangential flow u_x through an annulus of radial thickness Δy is written

$$(3/2)u_{\infty}\sin(x/r)2\pi\Delta y r\sin(x/r) = (3/2)u_{\infty} \cdot \sin(x_0/r)2\pi\Delta y_0 r\sin(x_0/r), \tag{C17}$$

which is solved to give

$$\Delta y = \Delta y_0[\sin(x_0/r)/\sin(x/r)]^2. \tag{C18}$$

For the cylinder, $\sin(x/r)$ is replaced by unity in expression (C18). Note that Δy is a function of x. Since x is a function of t (cf. expression (C15)), Δy is also a function of t. As the grid contracts according to expression (C18), the u_x values on the grid points are carried with the grid points. Hence the shear profile steepens with the contraction.

[60] The partial differential equation (C4) is computationally solved on the convecting-contracting grid using a time-centered implicit numerical scheme as outlined in Appendix 1 of *Borovsky et al.* [1981]. The grid extends from $y = 0$ to $y = y_{\max}$, with uniform (but time-dependent) gridspacing Δy. The boundary conditions are $u_x = 0$ at $y = 0$ and $u_x = u_{x0}$ (as given by expressions (C1) and (C2)) at $y = y_{\max}$. A typical grid has 10,000 grid points and it takes about 150,000 timesteps to convect the grid from the nose of the obstacle to the end of the cylinder.

[61] A convecting-contracting grid solution with $Re = 1 \times 10^4$ is shown in Figure 19. The derivative $\partial u_x/\partial y$ at $y = 0$ is calculated as a function of the grid-position x along the magnetosphere and this derivative is used in expression (C3) to obtain the viscous shear force per unit area on the magnetosphere τ, which is plotted as a function of the distance x from the nose of the magnetosphere. As can be seen in the figure, the shear stress τ is low at the nose (because the shear velocity is low there) and maximizes upstream of the terminator. Beyond the terminator the shear stress τ decreases with distance down the cylinder approximately as $x^{-1/2}$ as the boundary layer thickens and the gradients $\partial u_x/\partial y$ weaken.

[62] The total viscous shear force F_{visc} on the magnetosphere is obtained by integrating the shear force per unit area τ over the total surface area of the magnetosphere. For $\tau = \tau(x/r)$ this integral has the form

$$F_{\mathrm{visc}} = 2\pi r \int_0^{(\pi/2)r} \tau_h(x)\sin(x/r)dx + 2\pi r \int_{(\pi/2)r}^{(\pi/2)r+h} \tau_c(x)dx, \tag{C19}$$

where τ_h and τ_c are the shear stress on the surface of the hemisphere and of the cylinder regions, respectively. It is convenient and traditional to express the total viscous force in terms of a dimensionless coefficient of viscous drag C_{visc}, (cf. expression (8)). Expression (8) yields

$$C_{\mathrm{visc}} = F_{\mathrm{visc}}/\left[(1/2)\rho u_{\infty}^2\left(\pi r^2\right)\right]. \tag{C20}$$

[63] Running a series of convecting-contracting-grid numerical solutions to the viscous diffusion equation (C4) for various values of the Reynolds number Re, using the derivatives $\partial u_x/\partial y$ obtained in the numerical solutions to calculate the viscous stress $\tau(x)$ from expression (C3) and integrating $\tau(x)$ over the surface area of the magnetosphere according to expression (C19) to obtain the viscous drag force F_{visc} on the magnetosphere, the coefficient of viscous drag C_{visc} as a function of Re is obtained from expression (C20). This coefficient is then plotted in Figure 20. As can be seen, at higher Reynolds numbers (which is, at lower values of the kinematic viscosity ν_{kin}), the coefficient of viscous drag is less, so the viscous drag force on the obstacle is less. A fit to the simulation data points in Figure 20 yields

$$C_{\mathrm{visc}} = 13.3Re^{-1/2}. \tag{C21}$$

The reader is reminded that $Re = u_{\infty}d/\nu_{\mathrm{kin}}$.

[64] As a test of this method of calculating C_{visc}, when the integration of expression (C19) is carried out only over the hemisphere (from $x/r = 0$ to $x/r = \pi/2$), the viscous drag coefficient for the hemisphere is obtained as $C_{\mathrm{visc}} =$

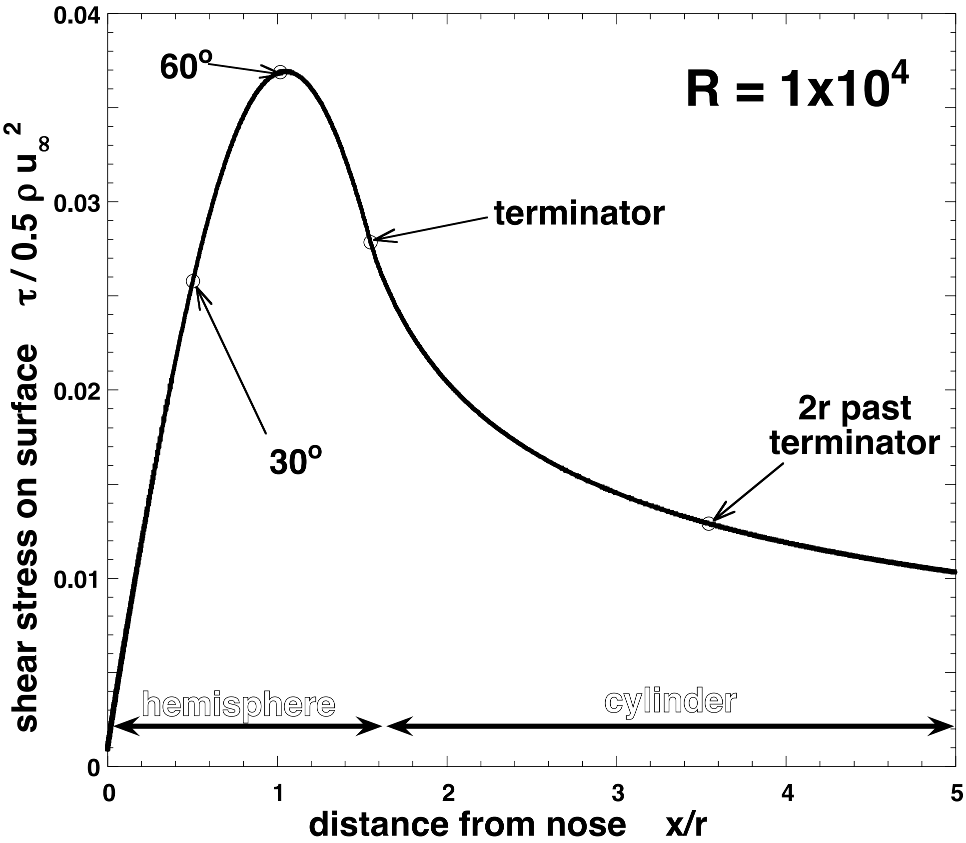

Figure 19. A computation of the viscous shear stress τ on the magnetosphere (normalized to $(1/2)\rho u_\infty^2$) is plotted as a function of the distance from the nose of the magnetosphere.

$6.8Re^{-1/2}$: this value agrees well with published calculations for the viscous drag of a sphere $C_{\rm visc} = 6.3Re^{-1/2}$ [*El-Shaarawi et al.*, 1997], which is approximately equal to the viscous drag of a hemisphere owing to boundary layer separation just behind the terminator ($\theta \approx 105°$). As a further test, turning off the grid compression but still using $u_{\rm grid} = 0.5u_{0x}$ for the grid velocity, this method yields $C_{\rm visc} = 1.59Re^{-1/2}$ for a flat-plate-shaped obstacle, which agrees well with theoretical solutions of the Navier-Stokes boundary layer equations for a thin flat plate. For the thin plate, this method would agree exactly with the Blassius theory $C_{\rm visc} = 1.33Re^{-1/2}$ (e.g., equation (2.5) of *Schlichting* [1979]) if $u_{\rm grid} = 0.35u_{0x}$ would be taken for the grid velocity and it would agree exactly with the parabolic-flow model $C_{\rm visc} = 1.46Re^{-1/2}$ (e.g., equation (9.18) of *Nakamura and Boucher* [1999]) if $u_{\rm grid} = 0.42u_{0x}$ would be taken for the grid velocity.

[65] Note that if there is slip at the surface of the obstacle owing to internal convection of the fluid obstacle, then $C_{\rm visc}$ is lower than that of expression (C20). Such a case is pertinent for the magnetosphere, as it is for liquid drops moving in air and for bubbles moving through fluids [e.g., *El-Shaarawi et al.*, 1997; *Juncu*, 1999]. The drag force is insensitive to the density ratio of the fluid obstacle to the exterior fluid [*Feng and Michaelides*, 2001]. Differences in the coefficient of viscous drag $C_{\rm visc}$ for solid spheres, liquid drops, and bubbles are about an order of magnitude at high Reynolds number [e.g., *Feng and Michaelides*, 2001].

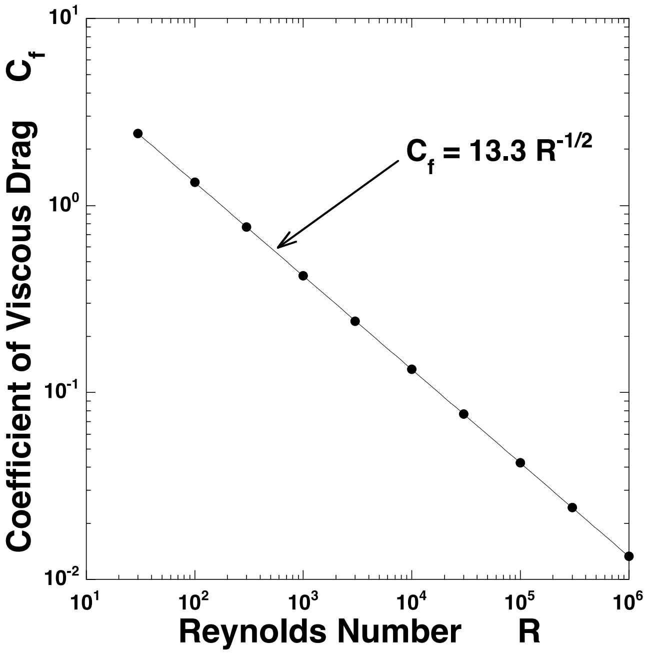

Figure 20. The coefficient of viscous drag for an obstacle shaped as a hemisphere of radius r followed by a cylinder of length $2r$ is plotted as a function of the Reynolds number $R = u_\infty d/\nu$. Each point is from a computation with a compressible grid convecting from the nose of the magnetosphere to the distance $2r$ past the terminator.

[66] **Acknowledgments.** The authors wish to thank Joachim Birn, Nick Borovsky, Bill Burke, Jack Gosling, and Chuck Smith for useful conversations. This work was supported by the NASA SR&T Program and the NSF GEM Program and was conducted with oversight from the U.S. Department of Energy.

[67] Arthur Richmond thanks the reviewers for their assistance in evaluating this paper.

References

Abramowitz, M., and I. A. Stegun (Eds.), *Handbook of Mathematical Functions*, Natl. Bur. of Stand., Washington, D. C., 1964.

Agullo, O., W.-C. Muller, B. Knaepen, and D. Carati, Large eddy simulation of decaying magnetohydrodynamic turbulence with dynamic subgrid-modeling, *Phys. Plasmas*, *8*, 3502, 2001.

Alfven, H., and C.-G. Falthammar, *Cosmical Electrodynamics*, Oxford Univ. Press, New York, 1963.

Antoine, Y., F. Lemoine, and M. Lebouche, Turbulent transport of a passive scaler in a round jet discharging into a co-flowing stream, *Eur. J. Mech. B Fluids*, *20*, 275, 2001.

Antonova, E. E., and I. L. Ovchinnikov, Equilibrium of the turbulent current and the current layer of the Earth magnetosphere tail, *Geomagn. Aeron., Engl. Transl.*, *36*(5), 7, 1996.

Armitage, P. J., Turbulence and angular momentum transport in a global accretion disk simulation, *Astrophys. J.*, *501*, L189, 1998.

Axford, W. I., Viscous interaction between the solar wind and the Earth's magnetosphere, *Planet. Space Sci.*, *12*, 45, 1964.

Balbus, S. A., and J. F. Hawley, Instability, turbulence, and enhanced transport in accretion disks, *Rev. Mod. Phys.*, *70*, 1, 1998.

Ballif, J. R., D. E. Jones, P. J. Coleman, L. Davis, and E. J. Smith, Transverse fluctuations in the interplanetary magnetic field: A requisite for geomagnetic variability, *J. Geophys. Res.*, *72*, 4357, 1967.

Ballif, J. R., D. E. Jones, and P. J. Coleman, Further evidence on the correlation between transverse fluctuations in the interplanetary magnetic field and Kp, *J. Geophys. Res.*, *74*, 2289, 1969.

Barriga, A. R., C. T. Crowe, and J. A. Robertson, Pressure distribution on a square cylinder at a small angle of attack in a turbulent cross flow, in *Wind Effects on Buildings and Structures*, p. 89, Cambridge Univ. Press, New York, 1977.

Batchelor, G. K., *An Introduction to Fluid Dynamics*, Cambridge Univ. Press, New York, 1970.

Bearman, P. W., Some effects of free-stream turbulence and the presence of the ground on the flow around bluff bodies, in *Aerodynamic Drag Mechanisms of Bluff Bodies and Road Vehicles*, edited by G. Sovran, T. Morel, and W. T. Mason, p. 95, Plenum, New York, 1978.

Belcher, S. E., T. M. J. Newley, and J. C. R. Hunt, The drag on an undulating surface induced by the flow of a turbulent boundary layer, *J. Fluid Mech.*, *249*, 557, 1993.

Bendat, J. S., and A. G. Piersol, *Random Data: Analysis and Measurement Procedures*, John Wiley, New York, 1971.

Bevington, P. R., and D. K. Robinson, *Data Reduction and Error Analysis for the Physical Sciences*, McGraw-Hill, New York, 1992.

Beyer, W. H., (Ed.), *Handbook of Tables for Probability and Statistics*, Chem. Rubber, Cleveland, Ohio, 1966.

Blair, M. F., Influence of free-stream turbulence on turbulent boundary layer heat transfer and mean profile development, part I, Experimental data, *J. Heat Transfer*, *105*, 33, 1983a.

Blair, M. F., Influence of free-stream turbulence on turbulent boundary layer heat transfer and mean profile development, part II, Analysis of results, *J. Heat Transfer*, *105*, 41, 1983b.

Bobrov, M. S., Kp index correlations with solar-wind parameters during the first and second stages of a recurrent geomagnetic storm, *Planet. Space Sci.*, *21*, 2139, 1973.

Borovsky, J. E., and J. T. Gosling, The level of turbulence in the solar wind and the driving of the Earth's magnetosphere, *Eos Trans. AGU*, *82*(20), Spring Meet. Suppl., S368, 2001.

Borovsky, J. E., C. K. Goertz, and G. Joyce, Magnetic pumping of particles in the outer Jovian magnetosphere, *J. Geophys. Res.*, *86*, 3481, 1981.

Borovsky, J. E., R. C. Elphic, H. O. Funsten, and M. F. Thomsen, The Earth's plasma sheet as a laboratory for flow turbulence in high-beta MHD, *J. Plasma Phys.*, *57*, 1, 1997.

Borovsky, J. E., M. F. Thomsen, and R. C. Elphic, The driving of the plasma sheet by the solar wind, *J. Geophys. Res.*, *103*, 17,617, 1998.

Braginskii, S. I., *Reviews of Plasma Physics*, edited by M. A. Leontovich, p. 205, Consult. Bur., N. Y., 1965.

Brucato, A., F. Grisafi, and G. Montante, Particle drag coefficients in turbulent fluids, *Chem. Eng. Sci.*, *53*, 3295, 1998.

Castro, I. P., and A. G. Robins, The flow around a surface-mounted cube in uniform and turbulent streams, *J. Fluid Mech.*, *79*, 307, 1977.

Chen, H., and D. Montgomery, Turbulent MHD transport coefficients: An attempt at self-consistency, *Plasma Phys. Controlled Fusion*, *29*, 205, 1987.

Cohen, J. E., and S. E. Belcher, Turbulent shear flow over fast-moving waves, *J. Fluid Mech.*, *386*, 345, 1999.

Cottet, G. H., Artificial viscosity models for vortex and particle methods, *J. Comput. Phys.*, *127*, 299, 1996.

Courchesne, J., and A. Laneville, An experimental evaluation of drag coefficients for rectangular cylinders exposed to grid turbulence, *J. Fluids Eng.*, *104*, 523, 1982.

Dennis, S. C. R., and J. D. A. Walker, Calculation of the steady flow past a sphere at low and moderate Reynolds numbers, *J. Fluid Mech.*, *48*, 771, 1971.

Duck, P. W., A. I. Ruban, and C. N. Zhikharev, The generation of Tollmien-Schlichting waves by free-stream turbulence, *J. Fluid Mech.*, *312*, 341, 1996.

El-Shaarawi, M. A. I., A. Al-Farayedhi, and M. A. Antar, Boundary layer flow about and inside a liquid sphere, *J. Fluids Eng.*, *119*, 43, 1997.

Eviatar, A., and R. A. Wolf, Transfer processes at the magnetopause, *J. Geophys. Res.*, *73*, 5561, 1968.

Faber, T. E., *Fluid Dynamics for Physicists*, Cambridge Univ. Press, New York, 1995.

Feng, Z.-G., and E. E. Michaelides, Drag coefficients of viscous spheres at intermediate and high Reynolds numbers, *J. Fluids Eng.*, *123*, 841, 2001.

Flesch, T. K., J. H. Prueger, and J. L. Hatfield, Turbulent Schmidt number from a tracer experiment, *Agric. For. Meteorol.*, *111*, 299, 2002.

Fontan, C. F., Turbulent MHD transport coefficients, *Plasma Phys. Controlled Fusion*, *41*, A635, 1999.

Freund, J. E., *Statistics a First Course*, Prentice-Hall, Old Tappan, N. J., 1981.

Fridman, E., Simulation of heat transfer from flow with high freestream turbulence to turbine blades, *J. Turbomach.*, *119*, 284, 1997.

Garrett, H. B., The role of fluctuations in the interplanetary magnetic field in determining the magnitude of substorm activity, *Planet. Space Sci.*, *22*, 111, 1974.

Garrett, H. B., A. J. Dessler, and T. W. Hill, Influence of solar wind variability on geomagnetic activity, *J. Geophys. Res.*, *79*, 4603, 1974.

Gatski, T. B., and T. Jongen, Nonlinear eddy viscosity and algebraic stress models for solving complex turbulent flows, *Prog. Aerosp. Sci.*, *36*, 655, 2000.

Goertz, C. K., L.-H. Shan, and R. A. Smith, Prediction of geomagnetic activity, *J. Geophys. Res.*, *98*, 7673, 1993.

Haerendel, G., Microscopic plasma processes related to reconnection, *J. Atmos. Terr. Phys.*, *40*, 343, 1978.

Hald, A., *Statistical Theory With Engineering Applications*, John Wiley, New York, 1952.

Hamba, F., Turbulent dynamo effect and cross helicity in magnetohydrodynamic flows, *Phys. Fluids A*, *4*, 441, 1992.

Hanjalic, K., and S. Kenjeres, T-RANS simulation of deterministic eddy structure in flows driven by thermal buoyancy and Lorentz force, Flow Turb, *Combustion*, *66*, 427, 2001.

Henkes, R. A. W. M., Scaling of the turbulent boundary layer along a flat plat according to different turbulence models, *Int. J. Heat Fluid Flow*, *19*, 338, 1998.

Hirshberg, J., and D. S. Colburn, Interplanetary field and geomagnetic variations—A unified view, *Planet. Space Sci.*, *17*, 1183, 1969.

Hoerner, S. F., *Fluid-Dynamic Drag*, chap. VI, Hoerner Fluid Dyn., Brick Town, N. J., 1965.

Hoffmann, J. A., Effects of freestream turbulence on the performance characteristics of an airfoil, *AIAA J.*, *29*, 1353, 1991.

Huang, R. F., and H. W. Lee, Effects of freestream turbulence on wing surface flow and aerodynamic performance, *J. Aircr.*, *36*, 965, 1999.

Hughes, W. F., and F. J. Young, *The Electromagnetodynamics of Fluids*, John Wiley, New York, 1966.

Jackson, J. D., *Classical Electrodynamics*, 2nd ed., John Wiley, New York, 1975.

Jeffreys, H., On the formation of water waves by wind, *Proc. R. Soc. London, Ser. A*, *107*, 189, 1925.

Juncu, G., A numerical study of steady viscous flow past a fluid sphere, *Int. J. Heat Fluid Flow*, *20*, 414, 1999.

Kamide, Y., and J. A. Slavin (Eds.), *Solar Wind-Magnetosphere Coupling*, Terra Sci., Tokyo, 1986.

Kenjeres, S., and K. Hanjalic, On the implementation of effects of Lorentz force in turbulence closure models, *Int. J. Heat Fluid Flow*, *21*, 329, 2000.

Koeltzsch, K., The height dependence of the turbulent Schmidt number within the boundary layer, *Atmos. Environ.*, *34*, 1147, 2000.

Krall, N. A., and A. W. Trivelpiece, *Prinicples of Plasma Physics*, McGraw-Hill, New York, 1973.

Lamb, H., *Hydrodynamics*, 6th ed., Cambridge Univ. Press, New York, 1932.

Leamon, R. J., C. W. Smith, N. F. Ness, W. H. Matthaeus, and H. K. Wong, Observational constraints of the dynamics of the interplanetary magnetic field dissipation range, *J. Geophys. Res.*, *103*, 4775, 1998.

Liemohn, M. W., J. U. Kozyra, M. F. Thomsen, J. L. Roeder, G. Lu, J. E. Borovsky, and T. E. Cayton, The dominant role of the asymmetric ring current in producing the stormtime Dst, *J. Geophys. Res.*, *106*, 10,883, 2001.

Littman, H., M. H. Morgan, and J. D. Paccione, A pseudo-Stokes representation of the effective drag coefficient for large particles entrained in a turbulent airstream, *Powder Tech.*, *87*, 169, 1996.

Makin, V. K., V. N. Kudryavtsev, and C. Mastenbroek, Drag of the sea surface, *Boundary Layer Meteorol.*, *73*, 159, 1995.

Mathieu, J., and J. Scott, *An Introduction to Turbulent Flow*, Cambridge Univ. Press, New York, 2000.

Matthaeus, W. H., and M. L. Goldstein, Measurement of the rugged invariants of magnetohydrodynamic turbulence in the solar wind, *J. Geophys. Res.*, *87*, 6011, 1982.

Mayaud, P. N., *Derivation, Meaning, and Use of Geomagnetic Indices*, AGU, Washington, D. C., 1980.

Miles, J., Surface-wave generation revisited, *J. Fluid Mech.*, *256*, 427, 1993.

Mishin, V. V., Viscous interaction of the solar wind with the Earth's magnetosphere and Kelvin-Helmholz instabilities, *Geomagn. Aeron. Engl. Transl.*, *19*, 634, 1979.

Mishin, V. V., On the MHD instability of the Earth's magnetopause and its geophysical effects, *Planet. Space Sci.*, *29*, 359, 1981.

Montgomery, D., Remarks on the mhd problem of generic magnetospheres and magnetotails, in *Magnetotail Physics*, edited by A. T. Y. Lui, p. 203, Johns Hopkins Univ. Press, Baltimore, Md., 1987.

Murakami, S., Overview of turbulence models applied in CWE-1997, *J. Wind Eng. Ind. Aerodyn.*, *74*, 1, 1998.

Murawaski, C. G., and K. Vafai, An experimental investigation of the effect of freestream turbulence on the wake of a separated low-pressure turbine blade at low Reynolds numbers, *J. Fluids Eng.*, *122*, 431, 2000.

Nakamura, Y., and R. F. Boucher, *Introduction to Fluid Mechanics*, chap. 9, Edward Arnold, London, 1999.

Neugebauer, M., and C. J. Alexander, Shuffling foot points and magnetohydrodynamic discontinuities is the solar wind, *J. Geophys. Res.*, *96*, 9409, 1991.

Nykyri, K., and A. Otto, Plasma transport at the magnetospheric boundary due to reconnection in Kelvin-Helmholtz vortices, *Geophys. Res. Lett.*, *28*, 3565, 2001.

Okamoto, M., Theoretical investigation of an eddy-viscosity-type representation of the Reynolds stress, *J. Phys. Soc. Jpn*, *63*, 2102, 1994.

Pagano, R. R., *Understanding Statistics in the Behavioral Sciences*, p. 137, West Publ., St. Paul, Minn., 1981.

Pal, S., Freestream turbulence effects on wake properties of a flat plate at an incidence, *AIAA J.*, *23*, 1868, 1985.

Papitashvili, V. O., N. E. Papitashvili, and J. H. King, Solar cycle effects in planetary geomagnetic activity: Analysis of 36-year long OMNI dataset, *Geophys. Res. Lett.*, *27*, 2797, 2000.

Parker, E. N., *Cosmic Magnetic Fields*, Clarendon, Oxford, 1979.

Pope, S. B., *Turbulent Flows*, Cambridge Univ. Press, New York, 2000.

Porter, D. H., and P. R. Woodward, High-resolution simulations of compressible convection using the piecewise-parabolic method, *Astrophys. J. Suppl. Ser.*, *93*, 309, 1994.

Reiff, P. H., T. W. Hill, and J. L. Burch, Solar wind plasma injection at the dayside magnetospheric cusp, *J. Geophys. Res.*, *82*, 479, 1977.

Roberts, D. A., M. L. Goldstein, and L. W. Klein, The amplitudes of interplanetary fluctuations: Stream structure, heliocentric distance, and frequency dependence, *J. Geophys. Res.*, *95*, 4203, 1990.

Rodi, W., Comparison of LES and RANS calculations of the flow around bluff bodies, *J. Wind Eng. Ind. Aerodyn.*, *69*, 55, 1997.

Rostoker, G., Geomagnetic indices, *Rev. Geophys. Space Phys.*, *10*, 935, 1972.

Safrankova, J., Z. Nemecek, O. Santolik, D. G. Sibeck, G. N. Zastenker, and A. Skalsky, The flank magnetopause: INTERBALL observations, *Adv. Space Res.*, *25*, 1503, 2000.

Schindler, K., On the role of irregularities in plasma entry into the magnetosphere, *J. Geophys. Res.*, *84*, 7257, 1979.

Schlichting, H., *Boundary Layer Theory*, McGraw-Hill, New York, 1979.

Sckopke, N., G. Paschmann, G. Haerendel, B. U. O. Sonnerup, S. J. Bame, T. G. Forbes, E. W. Hones, and C. T. Russell, Structure of the low-latitude boundary layer, *J. Geophys. Res.*, *86*, 2099, 1981.

Sears, W. R., On a boundary-layer phenomenon in magneto-fluid dynamics, *Astronaut. Acta*, *7*, 223, 1961.

Seeger, R. J., Fluid mechanics, in *Handbook of Physics*, 2nd ed., edited by E. U. Condon and H. Odishaw, chap. 2, McGraw-Hill, New York, 1967.

Shercliff, J. A., *A Textbook of Magnetohydrodynamics*, Pergamon, New York, 1965.

Smith, C. W., D. J. Mullan, N. F. Ness, R. M. Skoug, and J. Steinberg, Day the solar wind almost disappeared: Magnetic field fluctuations, wave refraction and dissipation, *J. Geophys. Res.*, *106*, 18,625, 2001.

Smits, A. J., and J.-P. Dussauge, *Turbulent Shear Layers in Supersonic Flow*, chap. 6, Am. Inst. of Phys., Woodbury, N. Y., 1996.

Smolentsev, S., M. Abdou, N. Morley, A. Ying, and T. Kunugi, Application of the ''K-ε'' model to open channel flows in a magnetic field, *Int. J. Eng. Sci.*, *40*, 693, 2002.

Snyder, C. H., M. E. Franke, and M. L. Masquelier, Wind-tunnel tests of an aircraft turret model, *J. Aircr.*, *37*, 368, 2000.

Sonett, C. P., and I. J. Abrams, The distant geomagnetic field, 3, Disorder and shocks in the magnetopause, *J. Geophys. Res.*, *68*, 1233, 1963.

Sonnerup, B. U. O., Theory of the low-latitude boundary layer, *J. Geophys. Res.*, *85*, 2017, 1980.

Sonnerup, B. U. O., K. D. Siebert, W. W. White, D. R. Weimer, N. C. Maynard, J. A. Schoendorf, G. R. Wilson, G. L. Siscoe, and G. M. Erickson, Simulations of the magnetosphere for zero interplanetary magnetic field: The ground state, *J. Geophys. Res.*, *106*, 29,419, 2001.

Spalart, P. R., Strategies for turbulence modelling and simulations, *Int. J. Heat Fluid Flow*, *21*, 252, 2000.

Speziale, C. G., Turbulence modeling for time-dependent RANS and VLES: A review, *AIAA J.*, *36*, 173, 1998.

Sutton, G. W., *Engineering Magnetohydrodynamics*, McGraw-Hill, New York, 1965.

Tennekes, H., and J. L. Lumley, *A First Course in Turbulence*, MIT Press, Cambridge, Mass., 1972.

Theobalk, M. L., P. A. Fox, and S. Sofia, A subgrid-scale resistivity for magnetohydrodynamics, *Phys. Plasmas*, *1*, 3016, 1994.

Torum, A., and N. M. Anand, Free span vibrations of submarine pipelines in steady flows: Effects of freestream turbulence on mean drag coefficients, *J. Energy Resour. Technol*, *107*, 415, 1985.

Townsend, A. A., *The Structure of Turbulent Shear Flow*, 2nd ed., Cambridge Univ. Press, New York, 1976.

Troishichev, O. A., V. G. Andrezen, S. Bennerstrom, and E. Friis-Christensen, Magnetic activity in the polar cap—A new index, *Planet. Space Sci.*, *36*, 1095, 1988.

Tsurutani, B. T., and W. D. Gonzalez, The cause of high-intensity long-duration continuous AE activity (HILDCAAs): Interplanetary Alfven waves, *Planet. Space Sci.*, *35*, 405, 1987.

Tsurutani, B. T., and W. D. Gonzalez, The efficiency of ''viscous interaction'' between the solar wind and the magnetosphere during intense northward IMF events, *Geophys. Res. Lett.*, *22*, 663, 1995.

Tsurutani, B. T., and C. M. Ho, A review of discontinuities and Alfven waves in interplanetary space: ULYSSES results, *Rev. Geophys.*, *37*, 517, 1999.

Tsurutani, B. T., W. D. Gonzalez, A. L. C. Gonzalez, F. Tang, J. K. Arballo, and M. Okada, Interplanetary origin of geomagnetic activity in the declining phase of the solar cycle, *J. Geophys. Res.*, *100*, 21,717, 1995.

Tu, C.-Y., and E. Marsch, MHD structures, waves, and turbulence in the solar wind, *Space Sci. Rev.*, *73*, 1, 1995.

White, W. W., J. A. Schoendorf, K. D. Siebert, N. C. Maynard, D. R. Weimer, G. L. Wilson, B. U. O. Sonnerup, G. L. Siscoe, and G. M. Erickson, MHD simulation of magnetospheric transport at the mesoscale, in *Space Weather*, edited by P. Song, H. Singer, and G. Siscoe, AGU, Washington, D. C., 2001.

Wu, J.-S., and G. M. Faeth, Effect of ambient turbulence intensity on sphere wakes at intermediate Reynolds numbers, *AIAA J.*, *33*, 171, 1994a.

Wu, J.-S., and G. M. Faeth, Sphere wakes at moderate Reynolds numbers in a turbulent environment, *AIAA J.*, *32*, 535, 1994b.

Wu, X., Generation of Tollmien-Schlichting waves by convecting gusts interacting with sound, *J. Fluid Mech.*, *397*, 285, 1999.

Volino, R. J., A new model for free-stream turbulence effects on boundary layers, *J. Turbomach.*, *120*, 613, 1998.

Yoshizawa, A., Self-consistent turbulent dynamo modeling of reversed field pinches and planetary magnetic fields, *Phys. Fluids B*, *2*, 1589, 1990.

Yoshizawa, A., Subgrid-scale modeling of magnetohydrodynamic turbulence, *J. Phys. Soc. Jpn*, *60*, 9, 1991.

Yoshizawa, A., and N. Yokoi, Stationary large-scale magnetic fields generated by turbulent motion in a spherical region, *Phys. Plasmas*, *3*, 3604, 1996.
Young, A. D., *Boundary Layers*, AIAA Educ. Ser., Washington, D. C., 1989.
Zdravkovich, M. M., and E. Carelas, Aerodynamics of a covered pedestrian bridge of a trapezoidal section, *J. Wind Eng. Ind. Aerodyn.*, *66*, 141, 1997.
Zelenyi, L., A. V. Milovanov, and G. Zimbardo, in *New Perspectives on the Earth's Magnetotail*, edited by A. Nishida, D. N. Baker, and S. W. H. Cowley, AGU, Washington, D. C., 1998.
Zhang, L., and J. C. Han, Combined effect of freestream turbulence and unsteady wake on heat-transfer coefficients from a gas turbine blade, *J. Heat Transfer*, *117*, 296, 1995.

J. E. Borovsky, Space and Atmospheric Science Group, Los Alamos National Laboratory, P.O. Box 1663, MS D466, NIS-1, SM-30 Bikini Atoll Road, Los Alamos, NM 87545, USA. (jborovsky@lanl.gov)
H. O. Funsten, Center for Space Science and Exploration, Los Alamos National Laboratory, Los Alamos, NM 87545, USA.